Effects of Varying Characteristic Injection Parameters and Geometric Configurations on the Cyclonic Flowfield in a Bidirectional Vortex **Chamber Using Velocity Inlet Conditions**

Gaurav Sharma* and Joseph Majdalani o Auburn University, Auburn, AL 36849

We vary the inflow properties in a finite-volume solver to investigate their effects on the computed cyclonic motion in a right-cylindrical vortex chamber. The latter comprises eight tangential injectors through which steady-state air is introduced under incompressible and inviscid conditions. To minimize cell skewness around injectors, a fine tetrahedral mesh is implemented first and then converted into polyhedral elements, namely, to improve convergence characteristics and precision. Once convergence is achieved, our principal variables are evaluated and compared using a range of inflow parameters. These include the tangential injector speed, count, diameter, and elevation. The resulting computations show that well-resolved numerical simulations can properly predict the forced vortex behavior that dominates in the core region as well as the free vortex tail that prevails radially outwardly, beyond the point of peak tangential speed. It is also shown that augmenting the mass influx by increasing the number of injectors, injector size, or average injection speed, further amplifies the vortex strength and all peak velocities while shifting the mantle radially inwardly. Overall, the axial velocity is found to be the most sensitive to vertical displacements of the injection plane. By raising the injection plane to the top half portion of the chamber, the flow character is markedly altered, and an axially unidirectional vortex is engendered, particularly, with no upward motion or mantle formation. Conversely, the tangential and radial velocities are found to be axially independent and together with the pressure distribution prove to be the least sensitive to injection plane relocations.

Nomenclature

total injection area A_i $A_{\rm inj}$ port area of individual injector Dchamber diameter F external body force gravity g L chamber length number of injectors $N_{\rm inj}$ normalized pressure pP static pressure normalized radial coordinate velocity of the fluid u normalized radial velocity u_r normalized swirl velocity u_{θ} normalized axial velocity u_z Vvortex Reynolds number normalized axial coordinate

radius of the chamber

Greek

a

β normalized discharge radius

off-swirl parameter

fluid molecular viscosity and density μ, ρ

modified swirl number

^{*}Graduate Research Assistant, Department of Aerospace Engineering, Member AIAA.

[†]Professor and Francis Chair, Department of Aerospace Engineering. Assoc. Fellow AIAA.

I. Introduction

THE MODELING of wall-bounded cyclonic flows continues to attract attention in a variety of phenomenological applications that extend from the smallest scales that accompany spinning electrons to the development of propulsive devices that are swirl driven [1–6]. The present study is motivated by one such propulsive application, namely, the so-called vortex engine concept. The latter is intended to leverage the improved flow stability, topology, overall efficiency, and self-cooling properties of internally swirled motions [1–11]. In fact, these swirl-induced flow attributes have often been shown to be effective at optimizing the design space, controllability margins, and stability of various power and thrust generation devices [8]. In this context, the bidirectional vortex engine design, introduced by Knuth and coworkers circa 1996, has led to the development of several prototypical engines that are fueled by either hybrid [1–3] or liquid propellants [4–6]. The concept of a bidirectional or bipolar vortex here refers to a cyclone chamber comprising a pair of coaxial, co-rotating inner and outer streams that remain separated by a rotating interfacial layer known as "mantle." These inner and outer streams are generally referred as the inner and outer vortex regions. In essence, the cyclonic motion gives rise to a rotating, non-translating "barrel" that permits the inward mass transport from the outer, low-temperature, annular vortex region to the inner, high-temperature, central vortex, thus helping to sustain dynamic mixing and effective thermal management [8].

Based on cylindrically-shaped cyclonic chamber configurations, inviscid models that describe the bulk internal steady-state motion in liquid-liquid rocket engines have been developed by several researchers [12–15]. A basic flow model for the so-called Vortex Injection Hybrid Rocket Engine (VIHRE), which is shown schematically in Fig. 1a, has also been advanced [16–18]. By way of confirmation, experimental cold-flow measurements of laboratory-scale vortex engines have been acquired using particle image velocimetry (PIV) and reported mainly for the swirl velocity and pressure distributions [19–23]. These data collections have been valuable in guiding the development of a constant shear stress model that produces realistic swirl velocities in the core region [24, 25]. Alternatively, using matched-asymptotic tools to capture the viscous core layer, a formulation that overcomes the singularity along the axis of rotation has been constructed [26].

In complementing the aforementioned theoretical investigations, finite-volume simulations that are dedicated to the vortex engine configuration have been performed under both cold [10] and reactive flow conditions [8]. The reactive simulations usually refer to either an academic prototype or a scaled-down model of the Vortex Combustion Cold-Wall (VCCW) chamber conceived by Chiaverini et al. [6]. The latter consists of a rather unconventional thrust chamber wherein the oxidizer is injected tangentially to the inner circumference, just upstream of the nozzle (see Fig. 1b). The low-temperature oxidizer then spirals around and climbs the chamber walls while filling the annular space between the mantle and the circumferential wall, i.e., the outer vortex region. Near the headwall, the oxidizer turns radially inwardly, reverses axial direction, and returns through the inner vortex after reacting with the fuel locally. Because of the fast mass transport through the annular region, the high-temperature reactants remain confined to the core vortex. In this manner, the underlying film cooling arrangement prevents the hot products from contacting the walls, thus serving as a protective thermal barrier that shields the walls against the high convective and radiative core temperatures [8].

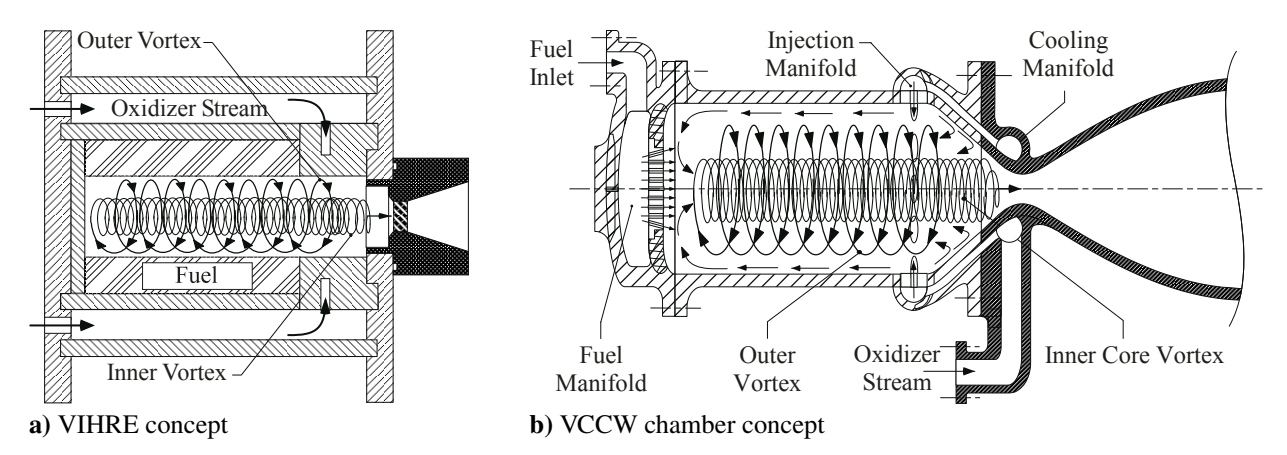


Fig. 1. Schematics of ORBITEC's a) Vortex Injection Hybrid Rocket Engine (VIHRE) conceived by Knuth et al. [2] and b) Vortex Combustion Cold-Wall (VCCW) chamber developed by Chiaverini et al. [6].

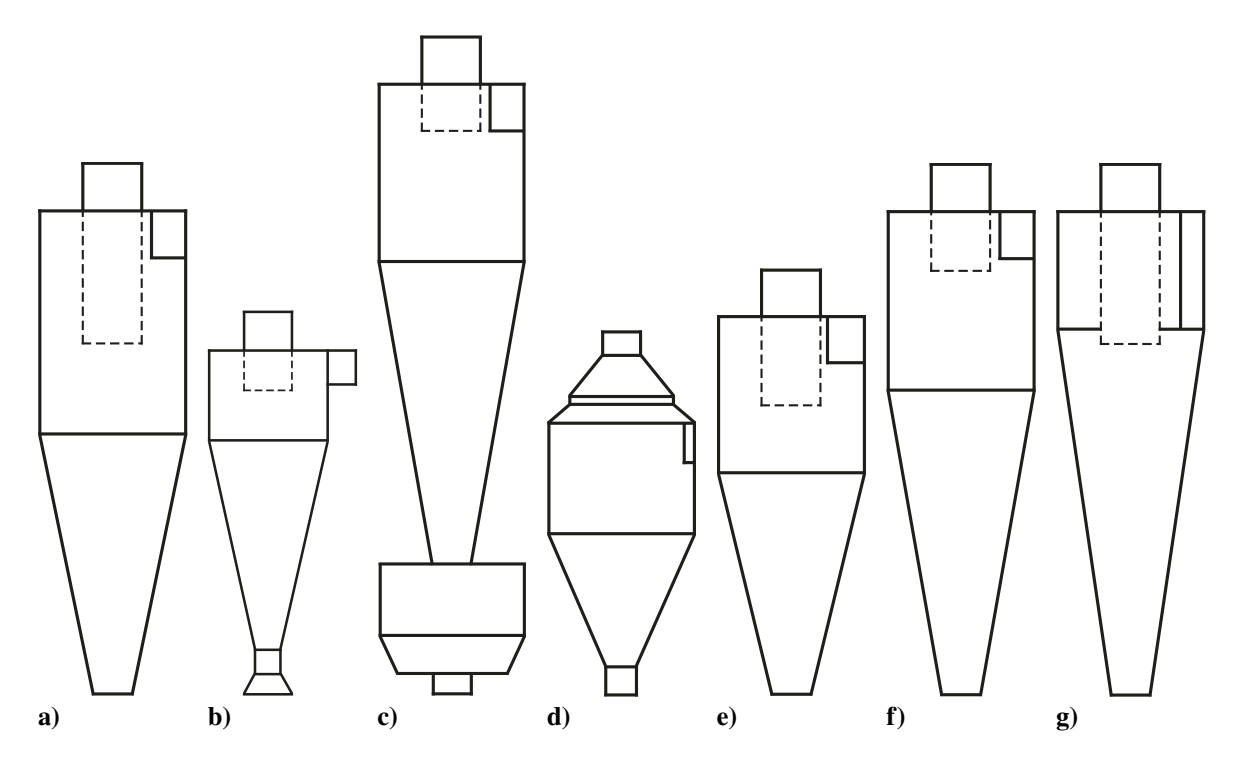


Fig. 2. Illustrations of various cyclone separator designs according to a) Shepherd and Lapple [27] (long vortex finder), b) ter Linden [30] (scroll inlet), c) Stairmand [31], d) Prockat [32] (no vortex finder), e) Peterson and Whitby [33], f) Swift [34], and g) Avant et al. [35] (long vortex finder and conical section).

Outside of propulsion, industrial cyclone separators and centrifuges may have been the first to leverage the unique properties that accompany the establishment of a wall-bounded, bidirectional vortex motion. Some of the earliest accounts of cyclonic fields, which focus on flow filtration rather than propulsion, can be traced back to experiments and semi-empirical studies of dust separators (see Fig. 2). For example, in their efforts to quantify the effects of dust loading on pressure drop characteristics, Shepherd and Lapple [27, 28] introduce an expansive cyclone separator circuit that captures velocities, pressures, frictional losses, vortical structures, and inlet variations (Fig. 2a). This is followed by a study that accounts for thermal effects on cyclonic variables [29]. In the interim, work by ter Linden [30] helps to characterize the effects of varying the length of the vortex finder on the efficiency of a cyclone separator (Fig. 2b). For optimal performance, Stairmand [31] designs two cyclone chambers that maximize either the mass flow rate or the efficiency of the separator (Fig. 2c). In fact, similar efforts are undertaken using several additional separator concepts that are outlined schematically in Figs. 2d–2g. Those begin with Prockat [32], who builds a cylinder-on-cone cyclone apparatus with a collection box in his quest to characterize a deduster's flow topology and dust collection performance (Fig. 2d). Peterson and Whitby [33] employ a modified Stairmand-type collector with nearly equally long cylindrical and conical sections to study the effect of particle size on dust separation efficiency (Fig. 2e). A proportionately longer conical section characterizes the cyclone configuration developed by Swift [34] (Fig. 2f), and this is further extended by Avant et al. [35], who manage to append a substantially longer vortex finder. The latter are concerned with the separation of cotton seeds from lint in what is known as a cotton ginning machine (Fig. 2g). Their conventional cyclone is found capable of achieving particle removal efficiency ranges of 60-75, 75-85, 85-90, and 100% for 2.5, 5, 10, and 20 µm sized particles, respectively.

As we shift from air to water as the working medium, several complementary works come to mind. Chief amongst them is a study by Kelsall [36] that introduces an ultramicroscope illumination method for measuring the tangential speed of aluminum particulates in a hydrocyclone. In this context, a miniaturized cylinder-on-cone apparatus made of cast acrylic walls is used to acquire measurements of both tangential and axial flow speeds, with the radial speed being recoverable from continuity. Kelsall [37] also provides auxiliary data that aids at quantifying the hydrocyclone's separation efficiency. Meanwhile, Fontein and Dijksman [38] concentrate on the pressure behavior and tangential velocity response, thus taking into account the relevance of a hydrocyclone to the ore and mining industries.

Shortly thereafter, in a two-part sequence of dedicated studies of hydrocyclones, Smith [39, 40] measures and

catalogues the vertical position of the mantle interface, where the axial speed vanishes, using a series of well-planned experiments. Despite the presence of a vortex finder that protrudes into his cyclone separator, the mantle location is seen to converge on two possible stations that consist of 62% and 72% of the chamber radius. These positions are later used to validate analytically-based theoretical findings that place the mantles at either 62.8% or 70.7%, depending on the helical model type [13, 14]. A decade later, Leith and Licht [41] manage to develop an empirical correlation for the collection efficiency that facilitates the design of high-efficiency gaseous separators. Leith and Mehta [42] also present and discuss several procedures to estimate the pressure drop and collection efficiency. By relying on comparisons to experimental measurements, these researchers identify a design optimization procedure that produces the most favorable pressure drop and efficiency in a cyclone separator.

As for the possible existence of multiple flow passes and corresponding mantles, Dabir and Petty [43] confirm that up to four reversals or countercurrents could occur in a hydrocyclone with a two-to-one vortex finder contraction. Using a flow visualization technique in conjunction with dye injection, these researchers help to ascertain that the average tangential velocity remains nearly independent of the axial station, as opposed to the axial velocity at the centerline, which varies linearly with elevation. In like fashion, Chu and Chen [44] use a particle dynamics analyzer to measure both radial and axial velocities as well as particle sizes and concentrations at various axial stations inside a transparent hydrocyclone.

Due to the evolution of hardware and the affordability of computing resources, numerical models continue to be pursued in the treatment of cyclonic flows. More specifically, numerical simulations of wall-bounded cyclone separators continue to experiment with different turbulence models and approaches in the hope of identifying the most effective closure equations for a swirl-dominated motion exhibiting highly anisotropic flow properties. Nonetheless, despite these sporadic efforts, numerical simulations of precession, flow instability, and breakdown remain largely unexplored. For example, a comprehensive numerical investigation of cyclone separators with air as the working fluid may be traced back to Hoekstra et al. [45]. Therein, diverse turbulence models are compared to experimental measurements and, ultimately, the Reynolds stress transport model is selected as the most realistic of the models examined. In a subsequent investigation, Derksen et al. [46] employ large eddy simulations (LES) to predict the fundamental features of a reverse-flow cyclone separator. This study proves to be particularly useful in providing a preliminary discussion of the precession pattern that can alter the inner vortex structure while destabilizing it. Derksen [47] extends this work further by applying his LES solver to predict the separation performance of a high-efficiency Stairmand-type cyclone using frozen-field, eddy-lifetime, and periodic-flow approaches. Moreover, by implementing two-way coupling with entrained particles, Derksen et al. [48] manage to incorporate the effects of two-phase flow into their computations. Meanwhile, Hu et al. [49] devise an accurate Reynolds stress model (RSM) that is substantially less costly than LES by modifying their production and convection modeled empirical constants for isotropization and by refining their pressure-strain model's wall-reflective term. Their three-dimensional calculations are subsequently corroborated using laser Doppler velocimetry (LDV) data in a cyclone separator. Many of these investigations are reviewed by Cortes and Gil [50], namely, in a comprehensive survey of reverse-flow cyclone separators, where the ability of each study to predict the tangential velocity distribution, pressure drop, and collection efficiency is systematically examined.

Efforts to improve the separation efficiency of cyclone separators continue to be undertaken using modern computational tools that are often based on Reynolds-averaged Navier–Stokes (RANS) and LES approaches. In this vein, Hussain et al. [51] evaluate the design and development of a flour mill cyclone separator at different injection speeds. Their simulations are performed for an air-dust mixture in a conventional cyclone separator. Similarly, Zabala–Quintero et al. [52] attempt a novel computational approach to predict the separation performance and pressure drop in a high-efficiency Stairmand-type cyclone separator. Therein, the Navier–Stokes equations are combined with the RSM turbulence relations in the treatment of the continuous phase while the Lagrangian approach is relied upon to track solid particles through the use of a one-way coupling paradigm. Along similar lines, Sayed et al. [53] present a full characterization of a Stairmand high-efficiency cyclone separator using a wall-modeled large eddy simulation (WMLES) at different Reynolds numbers. The corresponding algorithm follows an elliptic relaxation hybrid RANS/LES (ER-HRL) scheme to resolve the gaseous phase. Moreover, the wall-adjacent region is modeled using a linear eddy viscosity in conjunction with a RANS solver, while the bulk flow is captured using LES.

Despite the preponderance of numerical investigations of cyclone separators, only a few have been devoted to the right-cylindrical VCCW configuration using, for example, laminar, k- ε , and RSM models. Those that may be cited include those by Fang et al. [54], Anderson et al. [19], Murray et al. [55], Rom et al. [20], Maicke and Talamantes [56], Talamantes and Maicke [57], Majdalani and Chiaverini [8], Rajesh et al. [9], Sharma and Majdalani [10], and Evdokimov et al. [11]. To overcome this deficiency, and in complementing this line of inquiry, the present study will rely on a robust finite-volume solver to investigate the wall-bounded cyclonic motion in an idealized VCCW chamber.

In particular, this work will focus on performing cold-flow simulations of a cylindrical VCCW enclosure using different inlet conditions. To do so, the article will be organized as follows. First, the numerical methodology will be overviewed in Sec. II. Therein, the geometrical characteristics, mesh structure, baseline parameters, and conservation equations will be described. A table summarizing the parametric trade analysis campaign will also be provided. This will be followed in Sec. III with a detailed discussion of the results. These will begin with the velocity and pressure distributions for the problem's baseline case, and then extend to the effects of various inlet parameters. These will comprise the average injection speed, number of injectors, injector port diameter, and location of injectors. The study will conclude in Sec. IV with a summary of remarks and recommendations for future undertakings.

II. Numerical Methodology

We begin by devising a realistic model of the cyclonic chamber that can reproduce a motion that mimics the VCCW bulk flow. The objective here is to study the fundamental physics of the ensuing wall-bounded cyclonic motion under incompressible conditions assuming no chemical reactions or gaseous expansions. As such, no thrust performance characteristics will be predicted through this model. Rather, it will be used to identify cyclonic flow characteristics under inviscid conditions for the purpose of facilitating comparisons to those projected by fundamentally inviscid analytical solutions [12–15].

As shown in Fig. 3, a three-dimensional computational domain with eight protruding injectors can be used for an idealized rendition of the bidirectional vortex chamber. This two-part image includes an isometric view of the idealized vortex chamber in Fig. 3a as well as a side view in Fig. 3b depicting the key dimensions used in the simulations. Graphically, the axis of the chamber may be seen to coincide with the z-axis, which is measured downwardly, starting at the headwall.

Procedurally, the computational domain is first constructed in SolidWorks with the same dimensions used by Anderson et al. [19]. It is then meshed using a well-established gridding software called Integrated Computer Engineering and Manufacturing - Computational Fluid Dynamics (ICEM CFD). Afterwards, the discretized domain is imported into a finite-volume code, which is part of a commercial multiphysics package comprising an implicit, incompressible Navier–Stokes solver [58]. For the reader's convenience, the geometric details of the computational domain are provided in Table 1 and further outlined in Fig. 3b. These include the nominal dimensions for the length, chamber diameter, number of injectors, injector size, and total injection area for a baseline VCCW case.

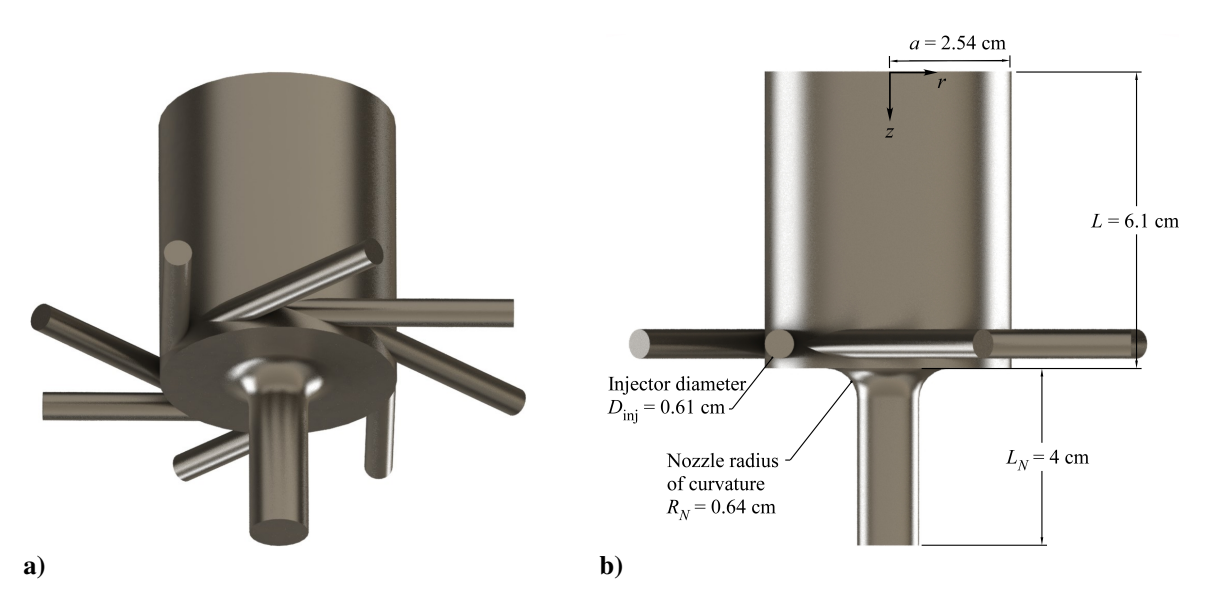


Fig. 3. Academic concept for a compact cyclonic chamber depicting a) isometric and b) side views of a right-cylindrical VCCW enclosure (baseline case).

Parameter Definition Value Units Chamber geometry \boldsymbol{L} 6.10 Chamber length cm D_c Chamber diameter (2a)5.08 cm Chamber outlet diameter (2b)2.54 cm L/D1.2 Length-to-diameter ratio Swirl injectors (aft-end) $N_{\rm inj}$ Number of injectors 8 $L_{\rm inj}$ Injector length 5 $D_{\rm inj}$ Individual port diameter 0.605 cm

0.2875

2.2998

cm²

 cm^2

Injection area of individual port

Total area of injection

Table 1. Geometric specifications of a lab-scale, cyclonic vortex engine.

A. Mesh Generation and Modeling Choices

 $A_{\rm inj}$

Given that the irregular geometry precludes the creation of a structured mesh, the most challenging aspect of this study may be to achieve a complete and effective unstructured mesh. The overarching difficulty may be attributed to the complications involved in resolving and refining the mesh in the region surrounding the tangential injectors as well as the sidewall. Due to highly acute angles between the injectors and the chamber wall, the mesh elements become highly skewed in these inflow regions. To minimize the ensuing mesh skewness, tetrahedral elements are carefully generated. This is carried out in conjunction with a mesher that evaluates the mesh quality by reporting zero for a high degree of skewness and unity for a perfect, unskewed element. When creating the mesh, the quality of the mesh is therefore prioritized and the process is repeated until the normalized quality of the mesh is seen to return a value above the minimum threshold of 0.3.

Recognizing that a tetrahedral mesh requires a relatively large number of elements to cover a given volume, one may decrease both computation time and power requirements by selecting a different gridding arrangement. In this work, by using the reverse Cuthill–McKee algorithm [59], the tetrahedral mesh elements over the VCCW domain are transformed into polyhedral mesh elements. As such, not only is the time to compute appreciably reduced, the solver's convergence properties are also markedly enhanced. Following this particular procedure, our simulation results become comparable in accuracy to those obtained using a fully structured hexahedral mesh albeit at a fraction of the cost [60]. For further clarity, a magnified view of the meshes near the injector and sidewall regions is presented in Fig. 4a, with the mesh topology being illustrated in Fig. 4b over the entire chamber and injector regions.

After generating the mesh and specifying the boundary types at all inlet and outlet sections, the mesh is readily imported into a robust finite-volume solver. Simulations are then performed using a steady, three-dimensional, segregated, and implicit framework. Computations are limited to a strictly inviscid model that embodies Euler's equations while permitting slip at the walls. Such requirements are imposed to facilitate the generation of stable and coherent cyclonic patterns that can be compared to analytical solutions that are derived under similar conditions [12–15].

B. Basic Nomenclature and Normalization

We find it useful to normalize all variables using the same reference values adopted in the corresponding theoretical formulations. This facilitates undertaking comparisons between simulation results and existing analytical solutions [12–15], namely, in an effort to guide their further refinement. Thus, using overbars to mark dimensional variables and the subscript "w" to imply a wall property, we proceed by setting:

$$z = \frac{\overline{z}}{a}, \quad r = \frac{\overline{r}}{a}, \quad u_{\theta} = \frac{\overline{u}_{\theta}}{U_{w}(z)}, \quad u_{z} = \frac{\overline{u}_{z}}{U_{w}(z)}, \quad u_{r} = \frac{\overline{u}_{r}}{U_{w}(z)}, \quad \text{and} \quad p = \frac{\overline{p}}{p_{w}}.$$
 (1)

In the above, \bar{r} and \bar{z} denote the radial and axial coordinates, p_w refers to the sidewall pressure, and $U_w(z) = u_\theta(1, z)$ stands for the swirl speed at the sidewall.

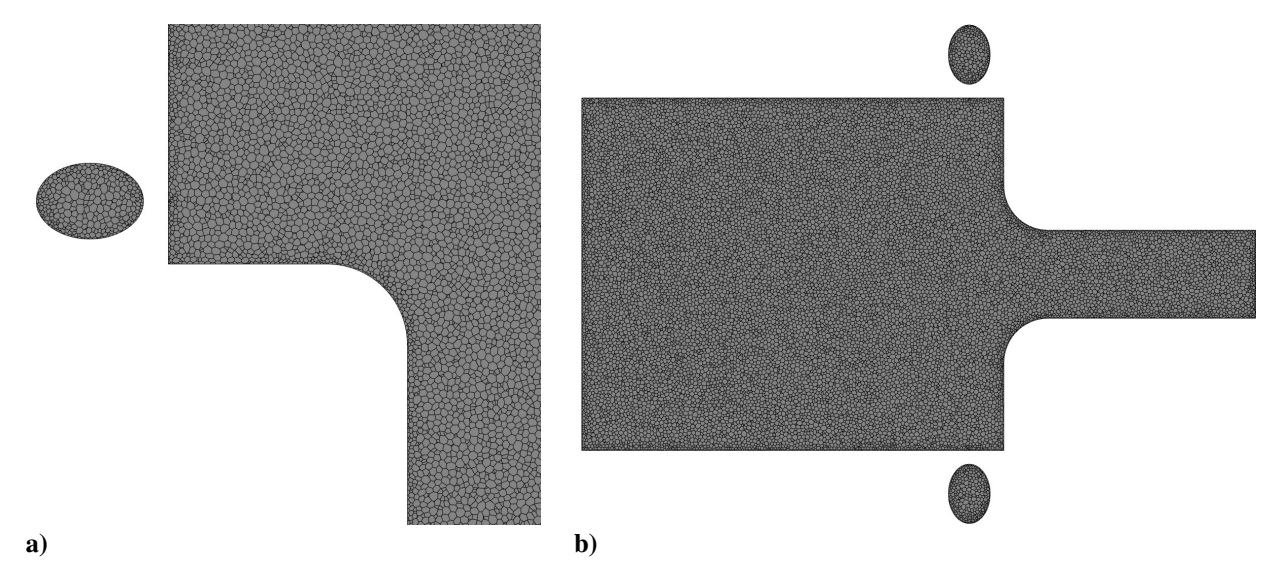


Fig. 4. Illustration of the chamber domain gridding topology using a) a magnified view of the polyhedral mesh elements and b) an inside view of the chamber with polyhedral mesh elements.

C. Conservation Equations

The continuity and momentum conservation equations that we use to model the VCCW cyclonic field follow from Euler's incompressible formulation. Using ρ and u to denote the fluid density and velocity, we have:

$$\nabla \cdot \boldsymbol{u} = 0 \qquad \text{(continuity)}, \tag{2}$$

$$\rho (\mathbf{u} \cdot \nabla) \mathbf{u} = -\nabla p + \rho \mathbf{g} + \mathbf{F} \qquad \text{(momentum conservation)}, \tag{3}$$

where p represents the static pressure, $\rho \mathbf{g}$ denotes the gravitational body force, and \mathbf{F} accounts for the effects of other external forces, such as the chamber's reaction forces acting on the fluid [58]. For simplicity, we use air as the working fluid, with a density of 1.177 kg/m³ at 26.85°C or 300 K.

As shown in previous work [10], it is possible to enhance the mesh and chamber configuration to the extent that all three velocity components can be robustly measured and characterized. Moreover, in several computational studies of the bidirectional vortex engine, the main emphasis is placed on describing the behavior of u_{θ} and p, with both u_r and u_z receiving secondary attention [19, 19–21, 24, 61]. Having managed to accurately resolve the velocity and pressure fields in similar configurations, we may now proceed to systematically explore the effect of modifying the injection velocity, number of injectors, injector diameter, and location of the injectors on the cyclonic flow properties. To this end, (1) the injection velocity, U_{inj} , (2) number of injectors, N_{inj} , (3) injector diameter, D_{inj} , and (4) location of the injector, z_{inj} , will be gradually varied while keeping all other parameters fixed.

As outlined in Table 2, a well-planned parametric trade analysis study can be conducted to determine how variations in the injector speed, size, number of injectors, and location of the injection plane can influence the VCCW cyclonic flowfield. To this end, a baseline configuration is selected that matches the chamber geometry used by Anderson et al. [19]. In conformance with the inviscid and incompressible flow assumptions, a uniform top-hat velocity profile of 60 m/s is prescribed as a plug flow at each injector inlet tube extending 5 cm tangentially to the chamber. The outlet pressure is also taken to be atmospheric. In order to couple the pressure and velocity variables, the semi-implicit method for pressure-linked equations (SIMPLE) algorithm [59] is used with the inlet being set as a velocity boundary condition. In this vein, the pressure is discretized using the so-called standard interpolation scheme while the momentum equations are discretized using a first-order upwind stencil. As the residuals stabilize during execution, and to achieve higher-order accuracy, the pressure is formulated using a second-order scheme, which is then followed by a second-order upwind technique in the momentum equation. The objective here is to prevent the sudden divergence of residuals that may be triggered by the high anisotropy, core singularity, and other geometric complexities that accompany cyclonic motions. Besides constructing scalars at cell faces, gradients are employed to compute secondary diffusion terms and velocity derivatives. Thus, using the gradient of variables, the terms associated with convection

Table 2. Parametric variation of different injection parameters.

Injection velocity, $U_{\rm inj}$ [m/s]	Number of injectors, $N_{\rm inj}$	Injector diameter, $D_{ m inj}$ [cm]	Location of injectors, z _{inj} [cm]		
10					
20					
30					
40					
50	8	0.605	$5.60 (z/L \approx 1)$		
60	0		3.00 (2/L ~ 1)		
70					
80					
90					
100					
	1				
	2		$5.60 \ (z/L \approx 1)$		
	3				
60	4	0.605			
00	5	0.003			
	6				
	7				
	8				
	8	0.200			
		0.250			
		0.300			
60		0.400	$5.60 (z/L \approx 1)$		
		0.500	3.00 (2/2 ~ 1)		
		0.605			
		0.700			
		0.740			
60	8		$0.300 \ (z/L \approx 0)$		
		0.605	$1.525 \ (z/L = 0.25)$		
			3.050 (z/L = 0.50)		
			$4.525 \ (z/L = 0.75)$		
			$5.600 \ (z/L \approx 1)$		

and diffusion in the flow conservation equations are discretized. In this work, the Green–Gauss cell-based scheme [59] is adopted in gradient calculations. Lastly, stringent convergence criteria are imposed to promote a sufficient degree of precision. More specifically, residuals are not permitted to exceed a 10^{-6} tolerance level in all three velocities along with the continuity equation. Aside from these convergence criteria, volume integrals of axial, radial, and tangential velocities are regularly evaluated and monitored to ensure proper convergence.

III. Results and Discussion

Computing the bulk gaseous motion in a bidirectional vortex engine can be invaluable at identifying the fundamental controlling parameters and in gaining a better understanding of the flow physics. In previous work [10], a parametric chamber outlet variation study has enabled us to isolate the effect of outflow properties, particularly, by modifying the nozzle inlet diameter and radius of curvature, on the three-component velocity field and pressure distributions. This was accomplished by varying the normalized chamber exit radius, $\beta \equiv b/a$, where b stands for the outlet radius, as well as the chamber's radius of curvature, R_N , which is specified in Fig. 3. The study proved effective at pinpointing the practical geometric requirements needed to mitigate the development of the so-called central recirculation zone (CRZ)

[62–64], namely, by preventing backflow from occurring. In the present sequel, the parametric trade analysis will be refocused on characterizing the effect of varying the inlet parameters (such as the injector velocity, count, diameter, and location) on the evolving flowfield.

Moreover, to properly correlate our computational results to existing analytical solutions, we have taken steps to ensure that the simulated parameters match most of their theoretical counterparts [12–15]. This includes, for instance, the modified swirl number,

$$\sigma \equiv \frac{a^2}{A_i},\tag{4}$$

where a and A_i represent the radius of the chamber and the total injection area, which are specified in Table 1 for the baseline case. Another useful metric consists of the off-swirl parameter [14], which appears naturally in analytical solutions. Given by

$$\kappa \equiv \frac{1}{2\pi\sigma} \frac{a}{L},\tag{5}$$

this Ekman-like number measures the importance of u_z/z and u_r relative to u_θ . With L referring to the chamber length in Table 1, a lower value of κ will generally imply a higher tangential-to-radial or tangential-to-axial velocity ratio.

In the interest of clarity, we begin by presenting illustrative simulations corresponding to the baseline case defined in Table 1, particularly, for an outlet fraction of $\beta = 0.5$ and an off-swirl parameter of $\kappa = 1/(2\pi \times 2.805) \times (2.54/6.1) = 0.0236$.

A. Velocity and Pressure Distributions for the Baseline Case

To prepare for the parametric inflow study, the baseline velocity and pressure distributions are computed and presented in Fig. 6. Note that the pressure distribution, normalized by its maximum value at r = 1, is illustrated in Figs. 5a and 5b. Here, the radial variation of p is computed at eight representative axial stations, starting at z/L = 0.1 (near the headwall), and ending at 0.8 near the outlet entrance region. The injection zone, where flow bending occurs, is deliberately avoided, being uncharacteristic of the idealized motion that we seek to capture. According to these results, the pressure gradient along the radius of the chamber remains nearly independent of the axial distance, particularly in Fig. 5a, although minor deviations appear around the axis of rotation.

As per theory, the pressure near the headwall, which corresponds to $r \ge 0.5$, must be slightly lower than the pressure near the injection site in order to assist in the upward convection of the incoming stream. Conversely, the pressure within the inner vortex has to decrease in the direction of outflow as z/L is increased from 0.1 to 0.8. This variation, which is captured numerically, seems to be minimal as we travel axially along a constant radius. In the case of Fig. 5b, a similar trend may be observed across the entire domain, where the axial invariance of the pressure is fundamentally confirmed. As a matter of fact, similar pressure distributions are reported by Hoekstra et al. [45], Hu et al. [49], Murray et al. [55], and Majdalani [14].

Next, we investigate the tangential velocity distribution in Fig. 5c, where the radial variation of u_{θ} is again illustrated at eight discrete axial stations, starting at z/L=0.1 near the headwall, and advancing by finite 0.1 intervals until a value of 0.8 is reached near the outlet section, which is judiciously avoided. To be consistent with theory and tradition, such as Rankine's free vortex lines, the tangential velocity is normalized using the tangential speed, $U_w(z) = u_{\theta}(1, z)$, taken at the respective z/L locations. This is shown in conjunction with the corresponding swirl velocity isocontours of Fig. 5d.

Forthwith, it may be seen that the swirl velocity is barely affected by the axial variation in Fig. 5c even with the use of a graphically elongated scale. In the vicinity of the injection site, however, the maximum swirl velocity will slightly exceed its value at the headwall, particularly, as u_{θ} begins to slowly recede while approaching the headwall. A more compelling demonstration of this axial invariance may be inferred from the u_{θ} isocontours; these appear to be relatively uniform along the length of the chamber, except for a very slight decrease in the width of the $(u_{\theta})_{\text{max}}$ isoband as z is increased. The foregoing observations are reassuring because they essentially support the axial invariance assumption that is frequently used in formulating the swirl velocity in several cyclonic flow studies [12–15]. In fact, based on the swirl velocity lines of Fig. 5c, one can further infer that a forced vortex motion prevails in the core region, where $u_{\theta} \to \Omega_{\text{forced}} r$ as $r \to 0$, a relation that implies solid body rotation at a circular speed of Ω_{forced} ; the profile then extends radially outwardly from the centerline to the point where $(u_{\theta})_{\text{max}}$ is reached. Shortly thereafter, this rotational region is succeeded by a free vortex motion with diminishing trailing lines that exhibit the inverted $u_{\theta} \approx r^{-1}$ form until a value of unity is attained at the wall.

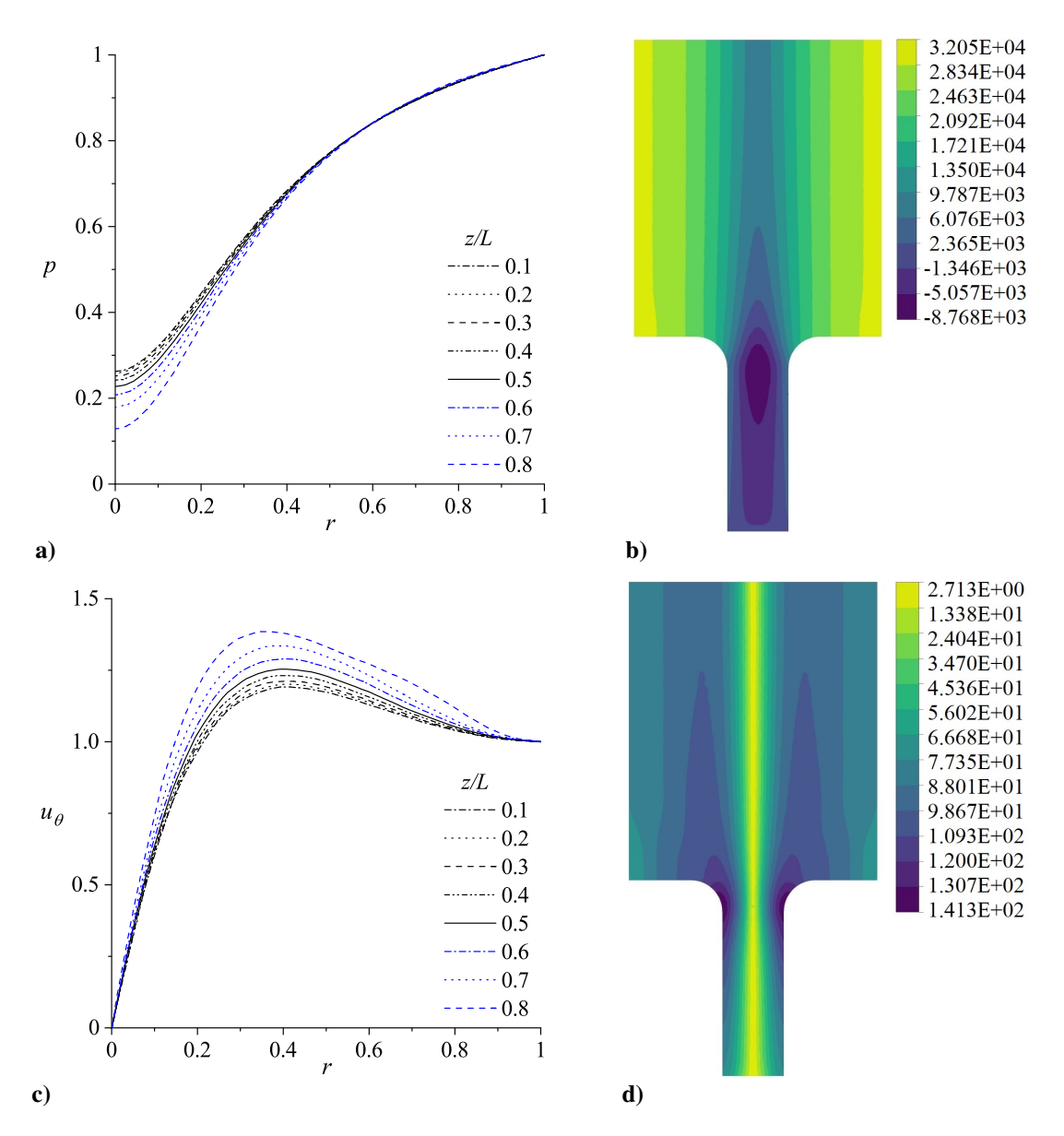


Fig. 5. Depiction of a) normalized pressure, b) pressure isocontours [Pa] c) normalized swirl velocity, and d) swirl velocity isocontours [m/s]. Plots provide radial distributions of the respective quantities at eight specific z/L locations while the isocontours are shown across a vertical r-z plane. Here $\beta = 0.5$ and $\kappa = 0.0236$.

As for the axial velocity's equispaced lines, these are shown in Fig. 6a, where the radial distribution of u_z , normalized using the tangential speed at the wall, $U_w(z)$, is depicted at eight different values of z/L. These are accompanied in Fig. 6b by isocontours of the u_z distribution throughout the chamber. Both graphs reflect a linear increase in the magnitude of u_z in the core region, specifically, as the fluid attempts to accelerate toward the outlet section. They also confirm the existence of two distinct regions that are composed of a core segment, where $u_z > 0$, and of an annular outer segment, where $u_z < 0$. For this baseline case, the axial polarity switches from a positive downward motion in the core region to a negative upward motion in the outer segment. This axial inversion occurs at $r \approx 0.504$, particularly, as u_z switches its sign past the midpoint of Fig. 6a. In practice, both "bidirectional" and "bipolar" designations may be attributed to the existence of these two adjacent and complementary segments, i.e., the inner and outer vortex regions with opposing polarities. As usual, separating these two flow segments is a rotating, but non-translating sheet or mantle, which is outlined using a solid line in Fig. 6b. The corresponding three-dimensional interface, which represents the locus of $u_z = 0$, appears as a surface of revolution with an average radius of $r \approx 0.504$.

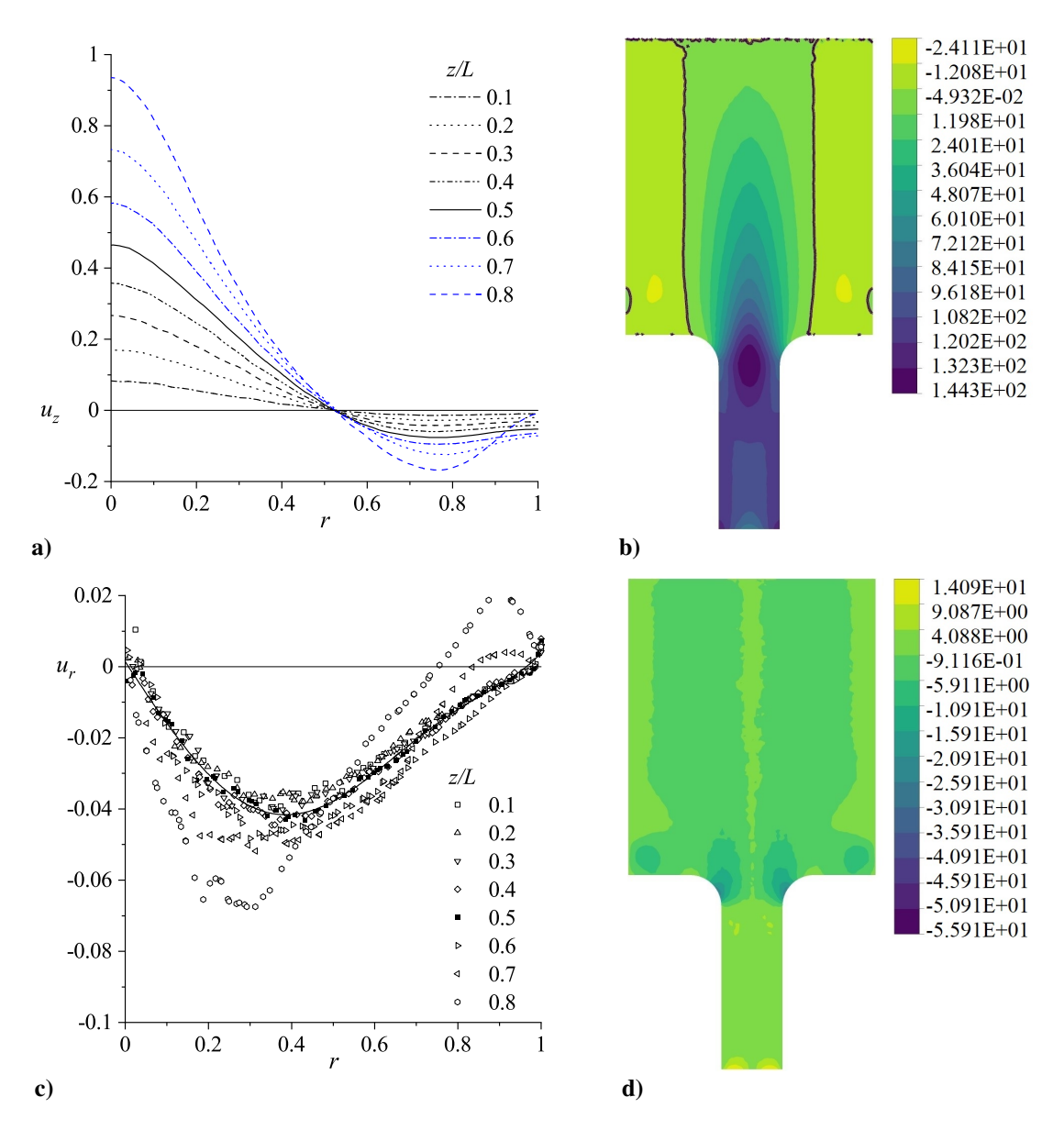


Fig. 6. Depiction of a) normalized axial velocity, b) axial velocity isocontours [m/s], c) normalized radial velocity, and d) radial velocity isocontours [m/s]. Plots provide radial distributions of the respective quantities at eight specific z/L locations while the isocontours are shown across a vertical r-z plane. Here $\beta = 0.5$ and $\kappa = 0.0236$.

Except for the minor bulging away from the nozzle, or the minor streamtube contraction that is observed as the nozzle is approached, the mantle's location remains consistent with theory as it nearly coincides with the fixed outlet radius of $\beta = 0.5$.

Finally, the normalized radial velocity distribution in the chamber is illustrated in Fig. 6c. For the reader's convenience, symbols are used to represent different axial stations, thus showcasing the statistical scatter of the solution around its average. Accordingly, the average radial velocity may be viewed as being qualitatively similar to the theoretical solution predicted by a family of analytical solutions [12–15]. This includes the presence of a maximum absolute value for $|u_r|$ that is off-centered with respect to the chamber radius. On this count, the solid line in Fig. 6c is used to designate the average radial velocity obtained for this baseline case using a polynomial fit to the scatter plot. As for Fig. 6d, it may be clearly seen that the complementary radial velocity isocontours confirm the same trends across the upper two-thirds of the domain where an axial invariance in u_r may be observed. Naturally, exceptions occur due to the strong flow turning activities that unfold in the immediate vicinity of the finite injectors and nozzle attachment,

i.e., in the chamber's lower quarter length, which likely account for the bulging and contraction of the contours. The axial invariance of the radial velocity is perhaps more evident in the isocontours of Fig. 6c than in the equispaced curves of Fig. 6c. Being a frequently used assumption in prescribing the form of u_r in cyclonic flow studies [12–15], the foregoing observations may be viewed as being fundamentally supportive of theoretical formulations associated with highly idealized axisymmetric flow configurations wherein the radial velocity is taken to be $u_r(r)$ only.

B. Effect of Inlet Parameters

Having showcased the capabilities of the numerically simulated flowfield at predicting all three components of the velocity and pressure, we now proceed to vary (1) the injection velocity, (2) the total number of injectors, (3) the injector port diameter, and (4) the injection site. With a fixed outlet fraction of $\beta = 0.5$, varying the inlet conditions

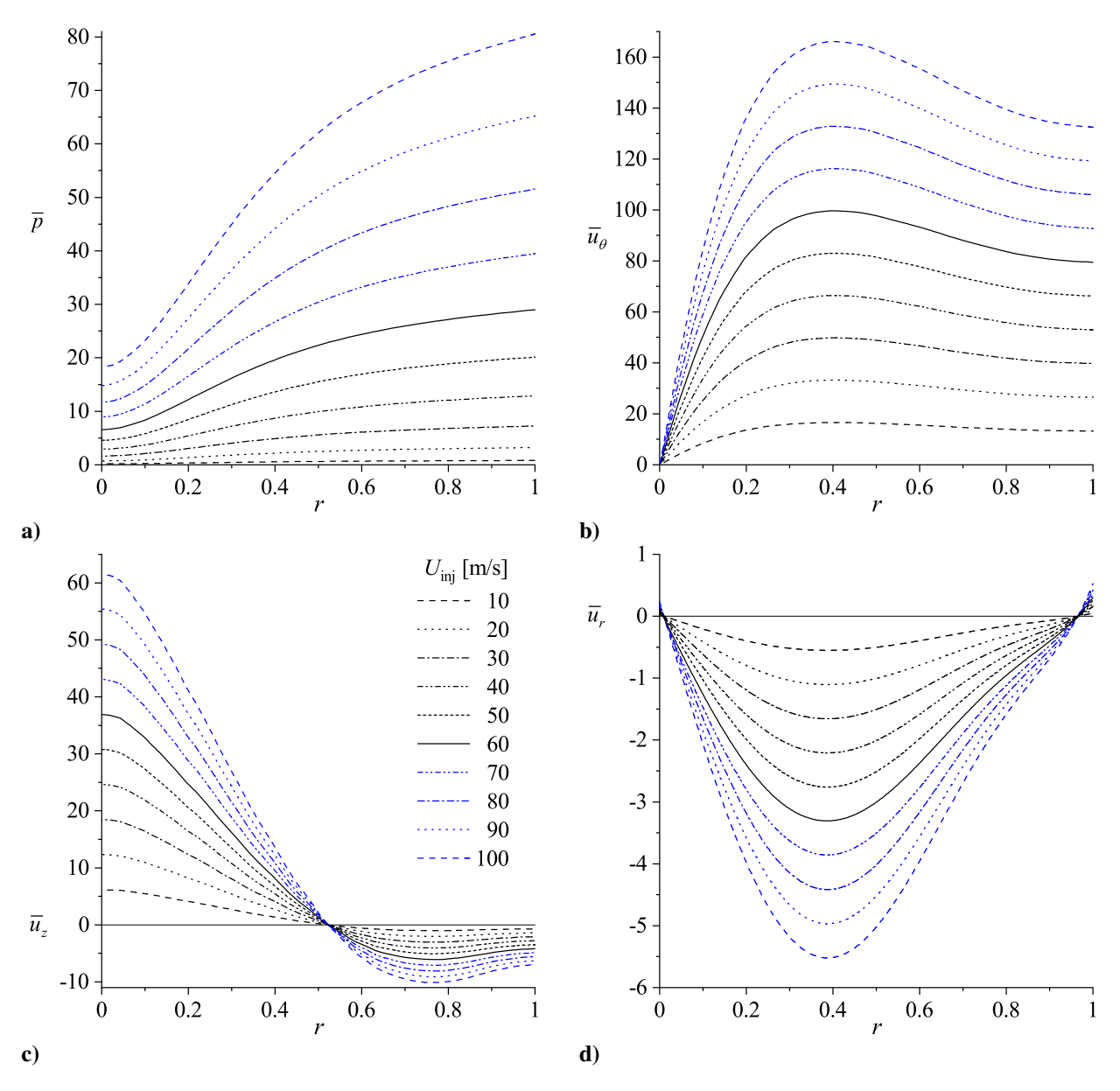


Fig. 7. Radial distribution of the a) pressure [kPa], b) swirl, c) axial, and d) radial velocities [m/s] at z/L = 0.5 and ten different injection speeds.

directly affects the injection mass flow rate. Having already explored the flow characteristics using the baseline values of $U_{\rm inj}=60$ m/s, $D_{\rm inj}=0.605$ cm, $N_{\rm inj}=8$, a=2.54 cm, b=1.27 cm, and L=6.1 cm, these specifications will serve as the control parameters for the remaining test cases. In this vein, we begin our numerical experimentation by varying the injection velocity, $U_{\rm inj}$, between 10 and 100 m/s, as shown in Fig. 7, where \overline{p} , \overline{u}_{θ} , \overline{u}_{z} , and \overline{u}_{r} are examined individually.

1. Injection Velocity

Since varying the injection speed directly affects the mass influx, the ensuing parametric analysis is aimed at pinpointing the influence of $U_{\rm inj}$ on the bulk flow character. Having already explored the flow behavior using a benchmark injection speed of 60 m/s, this value will serve as the control case. As shown in Fig. 7, we proceed by varying $U_{\rm inj}$ from 10 to 100 m/s in 10 m/s increments. In this effort, the control case is designated by a solid line and the maximum injection speed is set at 100 m/s, namely, to avoid venturing into the compressible regime. During this variation, the off-swirl parameter, κ , is kept constant at a value of 0.0236.

Forthwith, Fig. 7a showcases the pressure distribution at ten increasing values of the injection speed at a fixed axial station of z/L=0.5. It can be seen that the highest pressure near the wall corresponds to the case with the highest injection speed. The same may be said of the pressure gradients, which are most appreciable for $U_{\rm inj}=100$ m/s. Moreover, Fig. 7b illustrates the behavior of the inviscid form of the tangential velocity at various injection speeds and a fixed station of z/L=0.5. As expected, successive increments in $U_{\rm inj}$ serve to increase the peak swirl velocity throughout the chamber such that \overline{u}_{θ} is largest for $U_{\rm inj}=100$ m/s. This behavior is consistent with other confined cyclonic flow studies [10, 56].

Next, by switching to the axial velocity in Fig. 7c, one can infer that the peak $\bar{u}_z(0, z)$ (at the centerline) increases with successive increases in $U_{\rm inj}$. This behavior is consistent with continuity and concurrent with both numerical and theoretical findings [15, 56]. In the absence of viscous corrections, the magnitude of the axial velocity at the sidewall follows suit, and increases with $U_{\rm inj}$, as shown in Fig. 7c. A similar trend applies to the radial velocity, \bar{u}_r , which is characterized in Fig. 7d.

2. Number of Injectors

Under the current design and geometric constraints, the baseline case with eight injectors cannot be further extended because injectors will start to physically overlap with nine injectors or more. Instead, the number of injectors is reduced from eight to six, four, and two. Naturally, altering the injector count directly affects the total injection area, A_i , and thus modifies the off-swirl parameter κ . At the outset, κ may be seen to vary between the values of 0.0059 and 0.0236. In the interest of clarity, the actual values of κ , β , $(u_r)_{\min}$, r_{\min} , $(u_{\theta})_{\max}$, r_{\max} , and $(u_z)_{\max} \equiv u_z(0, L/2)$ are provided in Table 3 as a function of the injector count.

Returning back to the graphs, it may be seen that the shape of the equispaced pressure lines remains consistent across all three off-baseline cases. In comparison to the baseline case, the centerline values of the pressure may be seen to recede as the number of injectors is systematically decreased. As one may infer graphically from Fig. 8a, the chamber pressure remains directly proportional to the mass flow rate, which is expected of an incompressible solver. The increase in mass flow as the exit plane is approached results in both an increase in pressure and velocity. Since all

Table 3. Characteristic parameters for specific injector counts.

$N_{\rm inj}$	2	4	6	8	
К	0.0059	0.0118	0.0177	0.0236	
β	0.7420	0.6510	0.5650	0.5230	
$(u_r)_{\min}$	-0.0167	-0.0269	-0.0335	-0.0431	
r_{\min}	0.2776	0.2874	0.3034	0.4321	
$(u_{\theta})_{\max}$	1.0026	1.0419	1.1444	1.2535	
$r_{\rm max}$	0.9515	0.5609	0.4630	0.4064	
$(u_z)_{\text{max}}$	0.2264	0.3065	0.3802	0.4645	

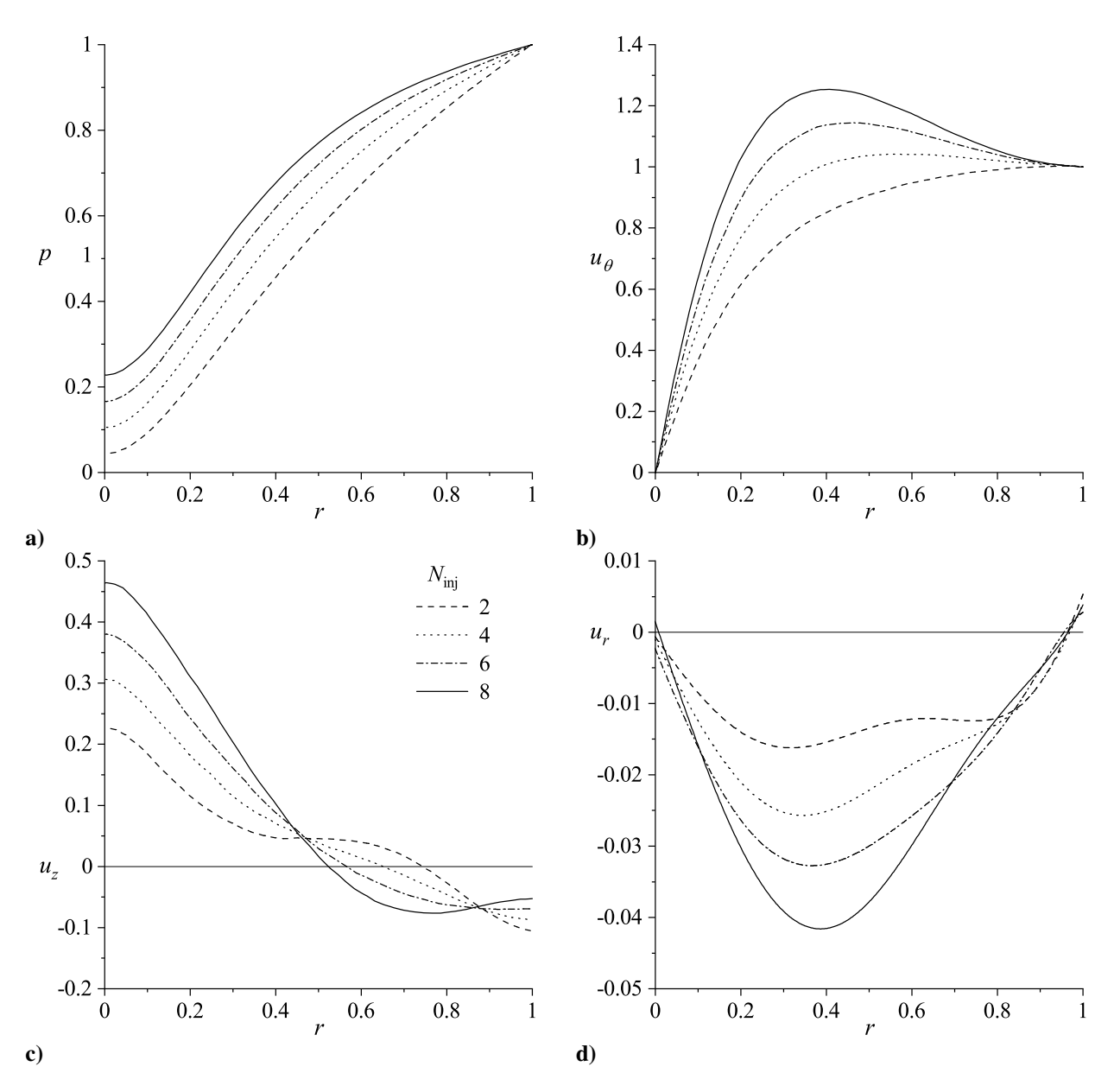


Fig. 8. Radial distribution of the normalized a) pressure, b) swirl, c) axial, and d) radial velocities at z/L = 0.5 and four different assortments of injector combinations ranging from $N_{\rm inj} = 2$ to 8.

models share the same chamber exit, a discrete reduction in the number of injectors leads to a corresponding decrease in mass influx. Consequently, the swirl velocity evolving in the chamber may be seen to somewhat diminish as compared to the baseline case; in particular, the peak enhancement observed near the centerline is substantially reduced, as per Fig. 8b. In short, the peak tangential speed $(u_{\theta})_{\text{max}}$, also known as the vortex strength, may be seen to decrease with successive decreases in N_{inj} . As shown in Table 3, $(u_{\theta})_{\text{max}}$ drops from approximately 1.25 with eight injectors to 1.00 with two injectors.

As for the axial velocity, it follows a similar linear decrease in its magnitude, as one may glean from Fig. 8c, especially at the centerline, as the flow courses its way out of the chamber. Irrespective of the asymmetries, flow recirculations, and irreversibilities that may occur around the injectors, the linear decrease in the mass flow rate that accompanies the uniform reduction in the injector count translates into a proportionate reduction in $(u_z)_{max}$ taken midway through the chamber. This behavior may be attributed to the mass eventually collecting around the centerline

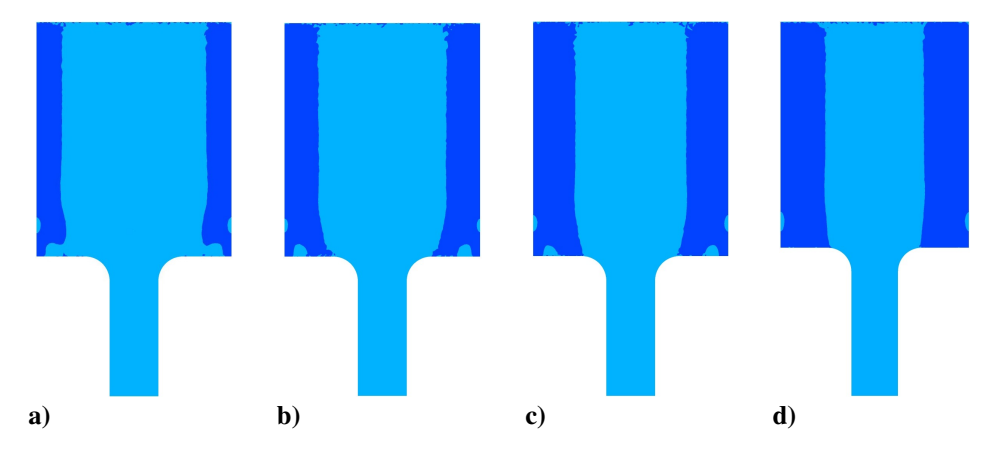


Fig. 9. Polarized axial velocity isocontours that showcase the computed mantle for four cases of $N_{\rm inj}$ corresponding to a) 2, b) 4, c) 6, and d) 8.

regardless of the manner by which it makes its entry into the chamber.

Interestingly, the behavior of u_z in the outer vortex region exhibits a peculiar trend, namely, one that is consistent with the mantle shifting outwardly from 0.523 in Table 3 to 0.565, 0.650, and 0.742, as $N_{\rm inj}$ is decremented. The outer shifting of the mantle and the corresponding shrinking of the flow passage in the outer vortex region may be attributed to the need to compensate for a smaller quantity of mass entering and filling the outer annular space separating the mantle from the wall. In fact, the corresponding expansion of the inner vortex diameter is clearly captured by the axial velocity isocontours provided through Fig. 9 for all four cases of $N_{\rm inj} = \{2, 4, 6, 8\}$. Therein, and everywhere thereafter, the darker shades in the contours are used to identify the flow moving toward the headwall whereas the lighter shades are used to mark the flow heading toward the exit plane. Despite $|u_z|$ in the outer region being the largest for the case of $N_{\rm ini}=2$, it eventually tapers down after crossing the mantle interface to a lower peak value at r=0 than any of its counterparts. These observations enable us to deduce the effect of the mass flow rate on the mantle displacement, a characteristic that we have been unable to capture in the outlet variation study [10]. By comparing the outcomes of the four injector counts on $|u_z|$, the peak centerline value may be seen to drop by 50% with each step-reduction in the number of injectors, and this behavior is reflected at all axial positions. A similar trend seems to affect the radial velocity, u_r , as its peak absolute value also diminishes in finite steps from 0.043 to 0.017 as $N_{\rm ini}$ is uniformly decreased from eight to two injectors (see Fig. 8d). This is accompanied by a leftward displacement of the locus r_{\min} of $(u_r)_{\min}$, which shifts from 0.43 to 0.28.

3. Injector Port Diameter

Besides the injector count, variables such as the injector port size can also influence the mass flow rate. In the upcoming trials, the injector diameters will be varied between 0.20 and 0.74 cm. As it will be shown, changing the inlet diameters has a direct bearing on A_i which, in turn, affects the modified swirl number σ , and therefore κ . A summary of the values considered for D_{inj} and their effect on (κ, β) as well as the peak velocities and their loci is provided in Table 4.

At this juncture, it should be noted that for the case of $D_{\rm inj} > 0.74$ cm, the individual port diameter becomes so large that the injectors start overlapping and producing a physically infeasible configuration. Conversely, reducing the diameter below 0.25 begins to destabilize the efflux, thus leading to the inception of backflow near the exit plane; the corresponding behavior will be illustrated for the case of $D_{\rm inj} = 0.2$ cm. To isolate the effect of the injector port size in our simulations, all other parameters will be held constant using their baseline values in Table 1. In the interest of brevity, we limit our attention in the remaining trials to the z/L = 0.5 station despite the availability of data at all axial locations. This midsection elevation is chosen as a reference station because the axial dependence of the computed results mirrors the previously discussed cases. Bearing these factors in mind, the outcomes of our simulations are summarized in Figs. 10 and 11.

Unsurprisingly, the normalized pressure distribution in Fig. 10a shows that the largest injector size produces the lowest pressure in the inner core region and the highest pressure differential between the wall region and the core.

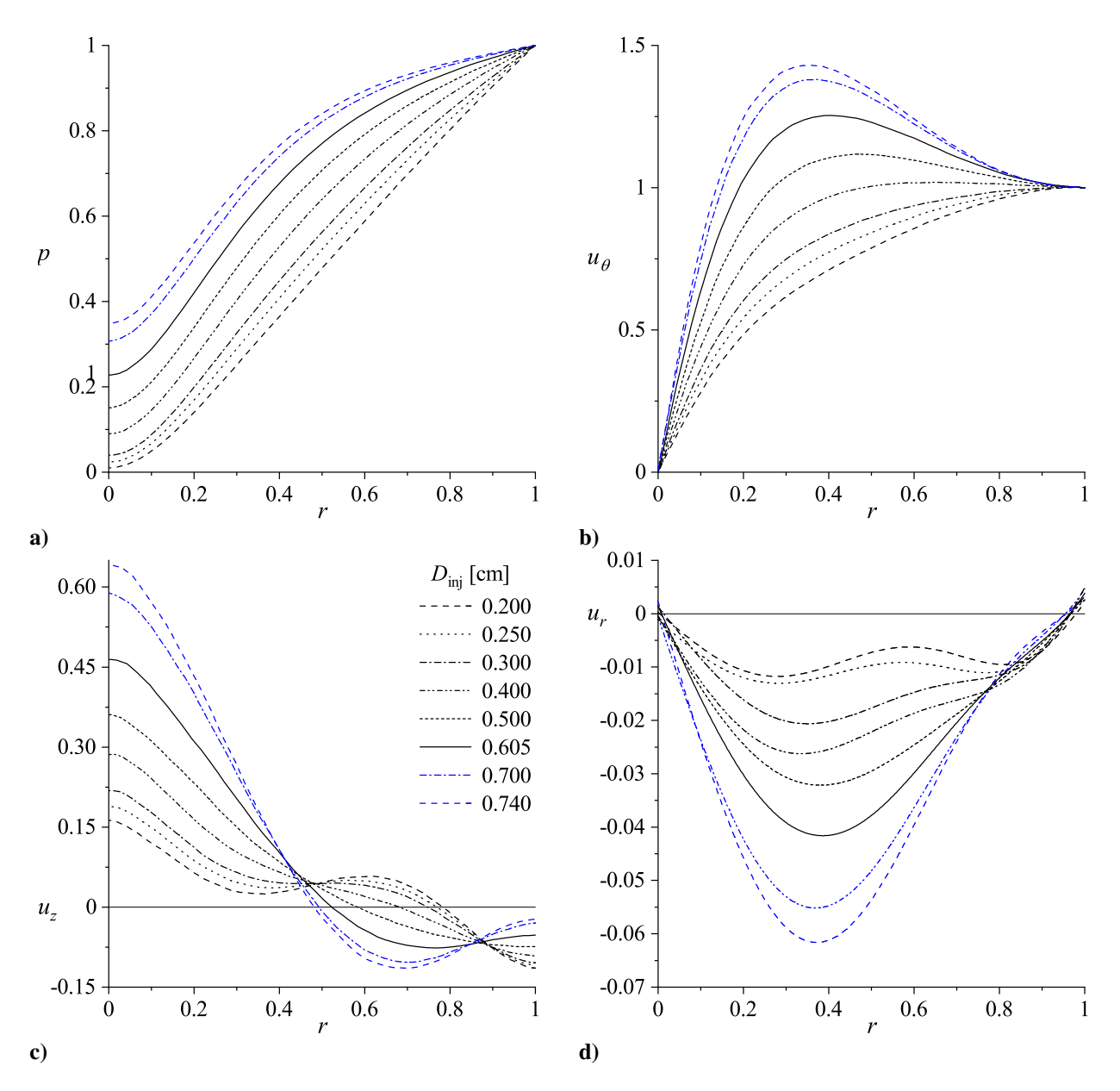


Fig. 10. Radial distribution of the normalized a) pressure, b) swirl, c) axial, and d) radial velocities at z/L = 0.5 and eight injector diameters.

The low pressure field engendered in the core can be attributed to both the increased swirl and axial velocities as the centerline is approached. Qualitatively, the pressure curves exhibit strong similarities and mirror their theoretical predictions [12–15].

The normalized swirl velocity, illustrated in Fig. 10b, shows that the injector diameter can have a substantial bearing on $(u_{\theta})_{\text{max}}$. Increasing the injector size increases the mass flow rate and, with it, the peak swirl velocities. These are found to increase from a value of unity at $D_{\text{inj}} = 0.2$ cm up to 1.43 at $D_{\text{inj}} = 0.74$ cm. The corresponding loci monotonically decrease from $r_{\text{max}} \approx 0.98$ near the wall to 0.36 for the largest port diameter. Here too, the u_{θ} profile resembles its theoretical formulation given by the Beltramian models [14, 15]. More specifically, it starts by reflecting a linearly varying swirl velocity of the form $u_{\theta} \approx \Omega_{\text{forced}} r$, which one associates with a forced vortex region evolving around the centerline. It is followed by a 1/r-type decay that is consistent with an irrotational (free vortex) tail past the peak u_{θ} value. However, as the injector size is reduced, the peak amplification near the centerline is also diminished.

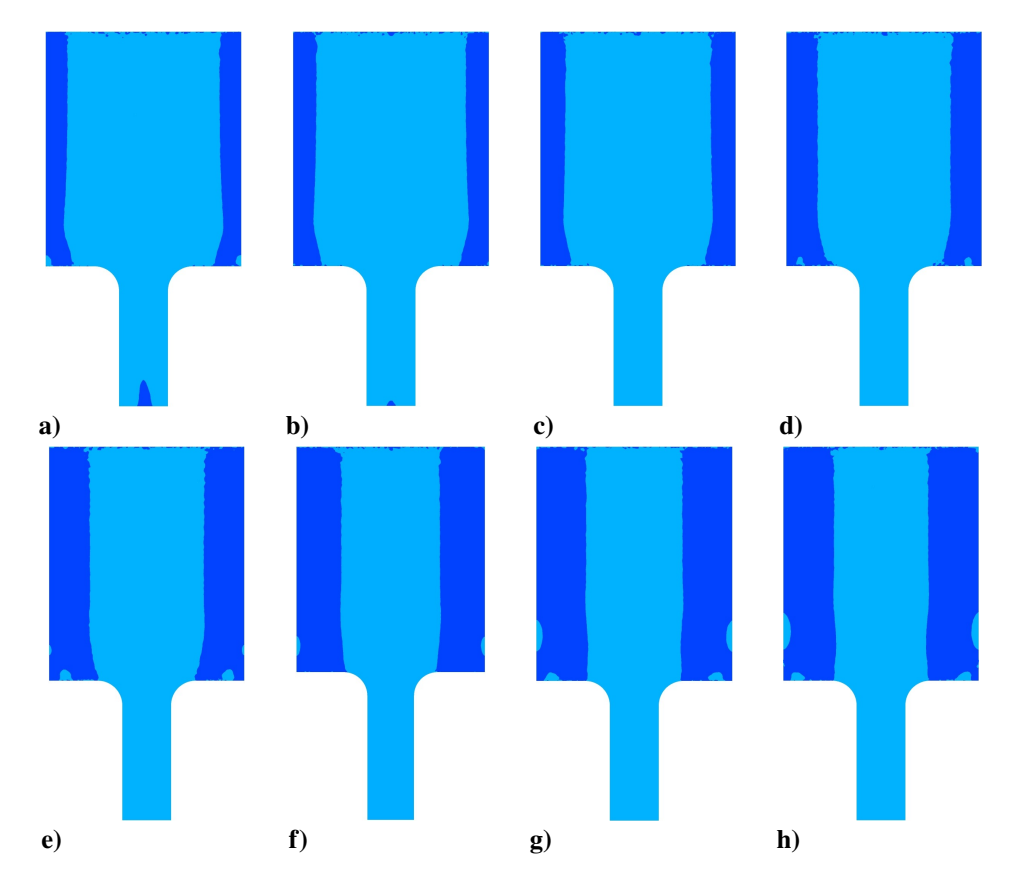


Fig. 11. Polarized axial velocity isocontours that showcase the computed mantle for eight cases of $D_{\rm inj}$ corresponding to a) 0.2 cm (backflow), b) 0.25 cm (lower limit), c) 0.3 cm, d) 0.4 cm, e) 0.5 cm, f) 0.605 cm (baseline), g) 0.7 cm, and h) 0.74 cm (upper limit).

The computed u_{θ} patterns remain consistent at the lower mass flow cases with their response to a smaller number of injectors as examined in Sec. III.B.2.

The axial velocity plots in Fig. 10c are equally affected by the progressive reduction in port diameter in a manner that is similar to that of reducing the number of injectors and, therefore, A_i . Due to continuity, a larger injector diameter gives rise to a larger mass influx and, subsequently, a magnification of u_z near the centerline. As shown in Table 4, the latter increases from 0.16 to 0.64 across the range of port diameters considered. The effect of expanding $D_{\rm inj}$ is therefore consistent with the use of a larger number of constant diameter injectors. Similar observations can be made of the radial velocity response to an increased mass influx, as reflected in Fig. 10d and Table 4. More specifically,

Table 4. Characteristic parameters for specific injector diameters.

D _{inj} [cm]	0.20	0.25	0.30	0.40	0.50	0.605	0.70	0.74
К	0.0026	0.0040	0.0058	0.0103	0.0161	0.0236	0.0316	0.0353
β	0.7840	0.7700	0.7480	0.6820	0.5810	0.5230	0.4920	0.4800
$(u_r)_{\min}$	-0.0127	-0.0137	-0.0185	-0.0218	-0.0322	-0.0431	-0.0578	-0.0598
r_{min}	0.1585	0.2051	0.2201	0.4263	0.3562	0.4321	0.3510	0.3393
$(u_{\theta})_{\max}$	1.0013	1.0027	1.0020	1.0187	1.1184	1.2535	1.3799	1.4306
$r_{\rm max}$	0.9758	0.9676	0.9736	0.6506	0.4631	0.4064	0.3759	0.3584
$(u_z)_{\text{max}}$	0.1628	0.1900	0.2186	0.2860	0.3608	0.4645	0.5892	0.6408

the peak radial velocity may be seen to increase from an absolute value of $|(u_r)_{\min}| \approx 0.013$ at $r_{\min} \approx 0.16$ to a value of 0.060 at $r_{\min} \approx 0.34$. As for the mantle sensitivity to the injector size, the shifting of the $u_z = 0$ interface may be clearly inferred from the axial velocity isocontours in Fig. 11, with the corresponding values of β being provided in Table 4 at eight different values of D_{inj} . In these simulations, β decreases from 0.784 at $D_{\text{inj}} = 0.20$ cm down to 0.48 at $D_{\text{inj}} = 0.74$ cm; the corresponding radial expansion of the outer annular segment serves to compensate for the increased flow rate pouring into the outer region.

4. Location of Injectors

In this last section, we explore the effect of relocating the injection plane on the flow development, which is captured through Figs. 12 and 13. This is accomplished by increasing the vertical elevation of the injection site from $z_{\text{inj}} = 0.3$

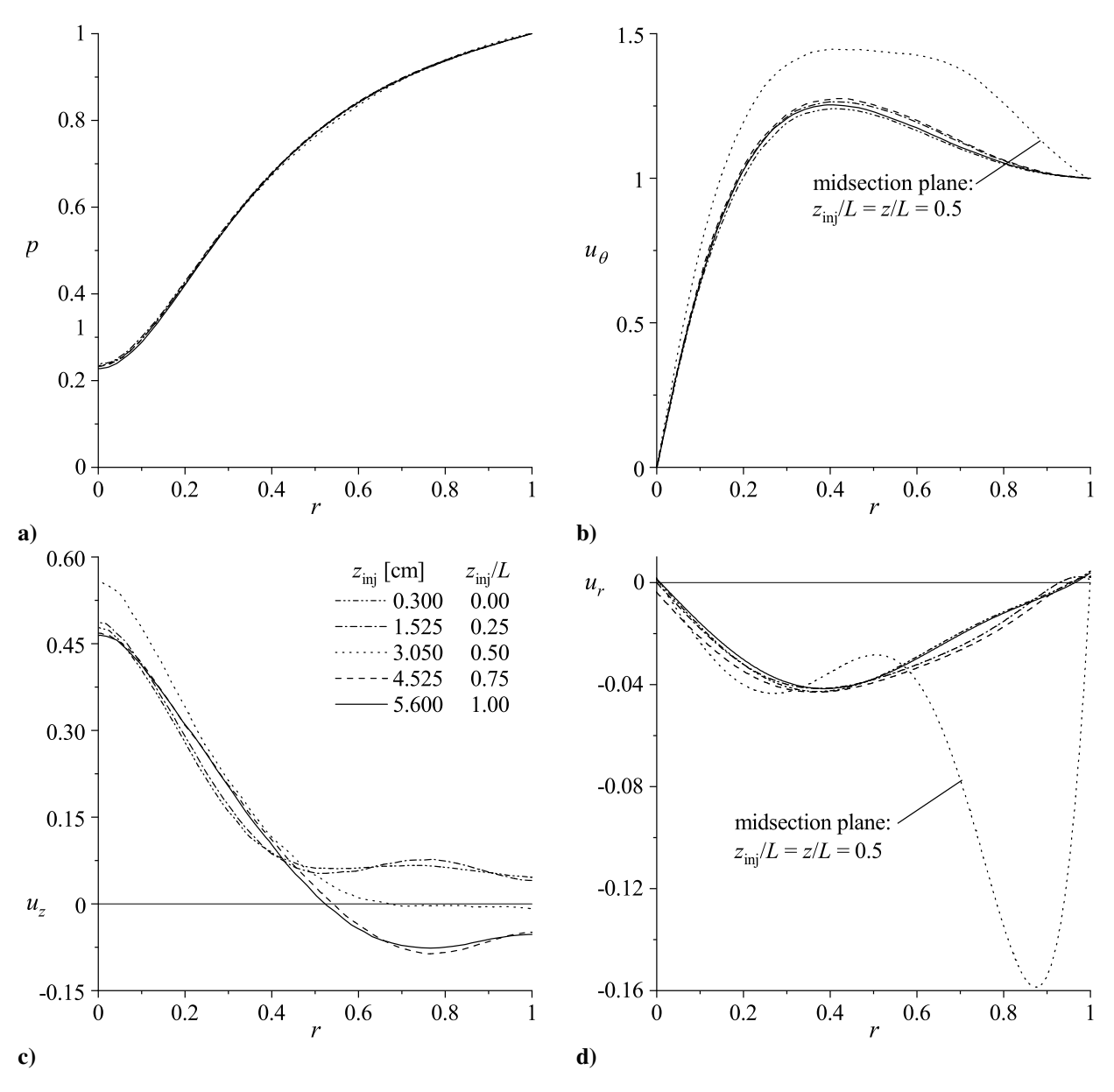


Fig. 12. Radial distribution of the normalized a) pressure, b) swirl, c) axial, and d) radial velocities taken at z/L = 0.5 using five different injector elevations.

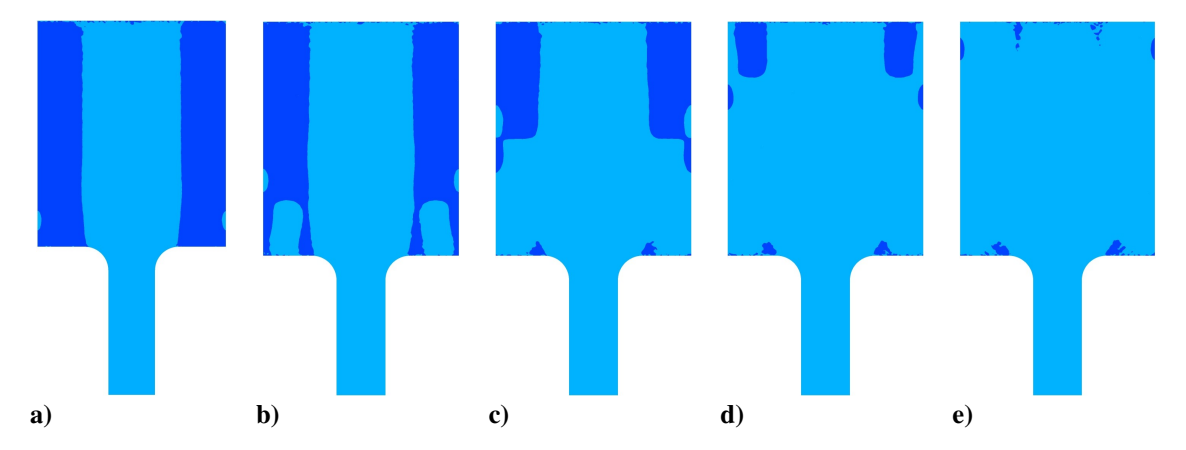


Fig. 13. Polarized axial velocity isocontours that showcase the computed mantle for five different injection sites corresponding to a) $z_{inj} = 5.6$ cm (endwall), b) 4.525 cm (quarter height), c) 3.05 cm (midsection), d) 1.525 cm (three-quarter height), and e) 0.3 cm (headwall).

cm to four additional stations spanning the length of the chamber, and ending near the endwall at $z_{inj} = 5.6$ cm. As opposed to previous permutations, this geometric variation does not alter the mass flow rate at entry, but rather the axial location of the injection plane.

Apart from the baseline case with $z_{\rm inj} = 5.6$ cm, simulation results at four additional injection heights are considered here: a slightly raised injection site at $z_{\rm inj} = 4.525$ cm, the chamber's quarter height when measured from the bottom, a midsection site at $z_{\rm inj} = 3.05$ cm, an injection site at three-quarters of the chamber height at $z_{\rm inj} = 1.525$ cm, and an injection site in the immediate vicinity of the headwall at $z_{\rm inj} = 0.3$ cm. Interestingly, we find that the pressure distribution, displayed in Fig. 12a, does not change by any appreciable amount irrespective of the injector placement. Moreover, except for the midsection injection case, the swirl velocity profile remains virtually invariant at four of the five cases examined in Fig. 12b. The uncharacteristic behavior that is observed using injection in the midsection plane can be attributed to all results, including the velocity profiles, being examined at the same z/L = 0.5 location. Around the injection site, the computed results are often smeared by inevitable flow turning and entrance effects. It is for this reason that the z/L = 0.5 station is selected as the ideal location for all other cases, namely, to avoid both flow entry and edge effects. As for the invariance of the swirl velocity with the injection site placement, it seems consistent with the theoretical solutions that invariably neglect the axial dependence of u_{θ} [12–15]. In some respect, raising the injection site has the equivalent effect of sliding the axial location at which swirl is imposed along the wall.

By switching our attention to the axial velocity distribution in Fig. 12c, one can infer that u_z exhibits the most sensitivity to variations in the injection site compared to other velocity components. For injection occurring below the midsection plane, the u_z curves do not quite differ as the injectors are raised. However a notable exception may be observed when injection takes place in the midsection plane. At this site, the axial velocity vanishes almost entirely, i.e., where the flow is being introduced, and where the three-dimensional flow turning into axial motion is actually initiated. Conversely, u_z in the inner core increases precipitously to the extent of slightly exceeding its centerline values for any other injection site. As for injection occurring in the top half of the chamber, the presence of a mantle gradually vanishes. Instead, the flow turns into an axially unidirectional vortex spiraling down the chamber with no upward motion. Interestingly, the flow becomes akin to a unidirectional vortex below the injection point even though the pressure distribution and both swirl and radial velocities remain unchanged. This behavior is also reflected by the axial velocity isocontours depicted in Fig. 13; clearly, the mantle remains visible only within the chamber segment extending between the injection site and the headwall.

Lastly, insofar as the normalized radial velocity is concerned, its profiles in Fig. 12d exhibit similar trends to those observed previously, or predicted by inviscid theory. Its invariance with the injection site is quite evident except for the case of midsection injection, which coincides with the plane in which the solution is displayed. At the point of injection, the tangential and radial components of the velocity dominate, as the flow attempts to negotiate a ninety degree turn and begin to develop an axial component. This explains the peak $|u_r|$ occurring when the injectors are located at z/L = 0.5.

IV. Concluding Remarks

Of the various computational studies that have undertaken the task of describing wall-bounded cyclonic flows, most have concentrated on industrial cyclone separators and centrifuges. A few have been specific to the bidirectional vortex motion associated with a Vortex Combustion Cold-Wall (VCCW) chamber configuration. Furthermore, parametric studies that examine the effect of varying injection properties on the ensuing flow character remain either scarce or inaccessible. For this reason, the main objective of this study has been to provide a dedicated characterization of the effect of changing the injection properties. This has been accomplished by altering the tangential injector average speed, injector port diameter, injector count, and injector location using a representative VCCW chamber.

By imposing slip-wall conditions in concert with an inviscid flow solver, this work helps to demonstrate that a judiciously constructed numerical model is capable of predicting the forced vortex behavior in the inner core region, as well as the free vortex motion that prevails in the outer region, consistently with theoretical predictions. These particular regions are well approximated analytically by a constant core shear stress model that allows for slip to occur at the wall. As long as the injection zone is avoided, the computational framework emulates to a certain degree the quasi-inviscid assumptions and results obtained by Maicke and Majdalani [24] for the tangential speed. Simulations of the axial and radial velocity profiles also agree with the theoretical patterns associated with exact analytical solutions of the inviscid Euler equations, particularly, those of the Beltrami type [14, 15].

Overall, this work helps to ascertain that a slip-permitting computational solver is somewhat effective at simulating the idealized pressure and velocity distributions, especially when the latter are displayed away from the chamber edges and inlet section. Moreover, the parametric trade analysis campaign shows that modifications of the inlet properties, $U_{\rm inj}$, $N_{\rm inj}$, $D_{\rm inj}$, and $z_{\rm inj}$, can have an appreciable impact on the swirl velocity, axial velocity, mantle location, flow polarity, and pressure distribution throughout the chamber. We find that, as the injection velocity is increased, the peak radial and tangential velocities are progressively augmented, with effects on $(u_{\theta})_{\text{max}}$ being the most pronounced. The pressure drop and axial velocity along the chamber axis are also amplified. As for the mantle location, it remains invariant to excursions in U_{ini} ; however, it does shift when the mass influx is altered by either modifying the number of injectors or their diameter. Next, we find that as the number of injectors is systematically reduced, so do the peak swirl velocity, axial velocity in the core region, and radial velocity. In contrast, the pressure gradient is found to increase as the injector count, $N_{\rm inj}$, is reduced. As for the mantle location, it shifts radially outwardly as the number of injectors is decreased and, with it, the rate of mass flow into the outer vortex region. In a sense, the effect of reducing the injector diameter appears to be analogous to that of reducing the number of injectors. Both lead to a lower mass influx, a narrowing of the outer vortex annular band, a decay in the peak velocities, a reduction in the vortex strength, and a rise in the radial pressure drop. Throughout these permutations, one also affirms the axial invariance of the tangential velocity and, to a lesser degree, the radial velocity, except when numerical measurements are taken near the plane of injection. Of the various parametric permutations considered, the most noticeable seem to follow our relocation of the plane of injection. Naturally, raising the injectors within the chamber leaves no trace on the mass flow rate or mantle station. However, it does have a substantial bearing on the evolving flowfield, especially when the injectors are raised to the top section of the chamber. For small vertical displacements away from the nozzle section, the pressure, swirl velocity, and radial velocity remain unchanged except when the injectors are relocated to the chamber's midsection plane. At such location, the results deviate from the idealized behavior due to surface inlet and flow turning effects. As the injectors are further relocated closer to the headwall, the axial velocity character changes altogether, thus leading to a unidirectional vortex spiraling downwardly while exhibiting no upward component. Naturally, the development of a strictly downward motion prevents the mantle interface from forming.

Now that the effect of each injection parameter has been somewhat clarified, it may be instructive to pursue a set of permutations of the dynamic flow control variables that depend, in large part, on the injection parameters considered here. Such simulations could be instrumental in identifying the threshold values of the non-dimensional group parameters that trigger the inception, precession, and breakdown of a wall-bounded cyclonic flow profile. In fact, such effort is presently underway and is hoped to be presented in forthcoming work.

Acknowledgments

This work was supported partly by the National Science Foundation, through grant № CMMI-1761675, and partly by the Hugh and Loeda Francis Chair of Excellence, Department of Aerospace Engineering, Auburn University. The authors are deeply indebted to Martin J. Chiaverini, Director of Propulsion Systems at Sierra Space Corporation, and to Donald Benner, Brian Pomeroy, and Arthur Sauer, for numerous technical exchanges and for their unwavering support.

References

- [1] Knuth, W. H., Bemowski, P. A., Gramer, D. J., Majdalani, J., and Rothbauer, W. J., "Gas-Fed, Vortex Injection Hybrid Rocket Engine," SBIR Phase I, NASA Final Technical Contract No. NAS8-40679, Madison, Wisconsin, August 1996.
- [2] Knuth, W. H., Gramer, D. J., Chiaverini, M. J., Sauer, J. A., Whitesides, R., and Dill, R., "Preliminary CFD Analysis of the Vortex Hybrid Rocket Chamber and Nozzle Flow Field," 34th AIAA/ASME/SAE/ASEE Joint Propulsion Conference and Exhibit, AIAA Paper 1998-3351, July 1998. doi:10.2514/6.1998-3351.
- [3] Knuth, W. H., Chiaverini, M. J., Sauer, J. A., and Gramer, D. J., "Solid-Fuel Regression Rate Behavior of Vortex Hybrid Rocket Engines," *Journal of Propulsion and Power*, Vol. 18, No. 3, May 2002, pp. 600–609. doi:10.2514/2.5974.
- [4] Chiaverini, M. J., Malecki, M., Sauer, J. A., Knuth, W. H., and Hall, C. D., "Vortex Combustion Chamber Development for Future Liquid Rocket Engine Applications," 38th AIAA/ASME/SAE/ASEE Joint Propulsion Conference and Exhibit, AIAA Paper 2002-4149, July 2002. doi:10.2514/6.2002-4149.
- [5] Sauer, J. A., Knuth, W. H., Malecki, M. J., Chiaverini, M. J., and Hall, C. D., "Development of a LOX/RP-1 Vortex Combustion Cold-Wall Thrust Chamber Assembly," 38th AIAA/ASME/SAE/ASEE Joint Propulsion Conference &: Exhibit, AIAA Paper 2002-4144, July 2002. doi:10.2514/6.2002-4144.
- [6] Chiaverini, M. J., Malecki, M., Sauer, J. A., Knuth, W. H., and Majdalani, J., "Vortex Thrust Chamber Testing and Analysis for O2-H2 Propulsion Applications," 39th AIAA/ASME/SAE/ASEE Joint Propulsion Conference and Exhibit, AIAA Paper 2003-4473, July 2003. doi:10.2514/6.2003-4473.
- [7] Numa, N. N., "Computational Analyses of Combustive Vortex Flows in Liquid Rocket Engines," *McNair Scholars Research Journal*, Vol. 2, No. 2, 2015, pp. 1–8.
- [8] Majdalani, J. and Chiaverini, M. J., "Characterization of GO2–GH2 Simulations of a Miniature Vortex Combustion Cold-Wall Chamber," *Journal of Propulsion and Power*, Vol. 33, No. 2, March 2017, pp. 387–397. doi:10.2514/1.b36277.
- [9] Rajesh, T. N., Jothi, T. J. S., and Jayachandran, T., "Performance Analysis of a Vortex Chamber Under Non-Reacting and Reacting Conditions," *Sādhanā*, Vol. 45, No. 1, February 2020, pp. 1–12. doi:10.1007/s12046-020-1271-1.
- [10] Sharma, G. and Majdalani, J., "Effects of Nozzle Inlet Size and Curvature on the Flow Development in a Bidirectional Vortex Chamber," *Physics of Fluids*, Vol. 33, No. 9, September 2021, pp. 093607. doi:10.1063/5.0066121.
- [11] Evdokimov, O., Prokhorov, D., Guryanov, A., and Veretennikov, S., "Transient Numerical Simulations of a Cold-Flow Bidirectional Vortex Chamber," *Physics of Fluids*, Vol. 34, No. 1, January 2022, pp. 015123. doi:10.1063/5.0079224.
- [12] Majdalani, J. and Rienstra, S. W., "On the Bidirectional Vortex and Other Similarity Solutions in Spherical Coordinates," *Zeitschrift für angewandte Mathematik und Physik*, Vol. 58, No. 2, September 2006, pp. 289–308. doi:10.1007/s00033-006-5058-y.
- [13] Vyas, A. B. and Majdalani, J., "Exact Solution of the Bidirectional Vortex," AIAA Journal, Vol. 44, No. 10, October 2006, pp. 2208–2216. doi:10.2514/1.14872.
- [14] Majdalani, J., "Helical Solutions of the Bidirectional Vortex in a Cylindrical Cyclone: Beltramian and Trkalian Motions," *Fluid Dynamics Research*, Vol. 44, No. 6, October 2012, pp. 065506. doi:10.1088/0169-5983/44/6/065506.
- [15] Majdalani, J., "Unified Framework for Modeling Swirl Dominated Helical Motions," 50th AIAA/ASME/SAE/ASEE Joint Propulsion Conference, AIAA Paper 2014-3677, July 2014. doi:10.2514/6.2014-3677.
- [16] Majdalani, J., Vortex Injection Hybrid Rockets, Chapter 6, Progress in Astronautics and Aeronautics. AIAA Progress in Astronautics and Aeronautics, Washington, DC, 2007, pp. 247–276.
- [17] Fleischmann, J. and Majdalani, J., "Complex Lamellar Helical Solution for Cyclonically Driven Hybrid Rocket Engines," 53rd AIAA Aerospace Sciences Meeting, AIAA Paper 2015-0372, January 2015. doi:10.2514/6.2015-0372.
- [18] Marquardt, T. A. and Majdalani, J., "Beltramian Solution for Cyclonically Driven Hybrid Rocket Engines," 53rd AIAA/SAE/ASEE Joint Propulsion Conference, AIAA Paper 2017-4638, July 2017. doi:10.2514/6.2017-4638.
- [19] Anderson, M. H., Valenzuela, R., Rom, C. J., Bonazza, R., and Chiaverini, M. J., "Vortex Chamber Flow Field Characterization for Gelled Propellant Combustor Applications," 39th AIAA/ASME/SAE/ASEE Joint Propulsion Conference and Exhibit, AIAA Paper 2003-4474, Huntsville, AL, July 2003. doi:10.2514/6.2003-4474.

- [20] Rom, C. J., Anderson, M. H., and Chiaverini, M. J., "Cold Flow Analysis of a Vortex Chamber Engine for Gelled Propellant Combustor Applications," 40th AIAA/ASME/SAE/ASEE Joint Propulsion Conference and Exhibit, AIAA Paper 2004-3359, July 2004. doi:10.2514/6.2004-3359.
- [21] Rom, C. J., Flow Field and Near Nozzle Fuel Spray Characterizations for a Cold Flowing Vortex Engine, Masters thesis, University of Wisconsin Madison, May 2006.
- [22] Khan, O. and Ahmed, A., "Modification of Jet Exiting a Cyclone Chamber," AIAA Scitech 2020 Forum, AIAA Paper 2020-0813, January 2020. doi:10.2514/6.2020-0813.
- [23] Khan, O., An Experimental Investigation of Confined Cyclonic Flows and Ensuing Jet, Ph.D. dissertation, Auburn University, Auburn, Alabama, May 2021.
- [24] Maicke, B. A. and Majdalani, J., "A Constant Shear Stress Core Flow Model of the Bidirectional Vortex," *Proceedings of the Royal Society A: Mathematical, Physical and Engineering Sciences*, Vol. 465, No. 2103, March 2009, pp. 915–935. doi:10.1098/rspa.2008.0342.
- [25] Maicke, B. A. and Majdalani, J., "Inviscid Models of Cyclonically Driven Internal Flows," *International Journal of Energetic Materials and Chemical Propulsion*, Vol. 15, No. 4, 2016, pp. 305–324. doi:10.1615/intjenergeticmaterialschemprop.2016016511.
- [26] Majdalani, J. and Chiaverini, M. J., "On Steady Rotational Cyclonic Flows: The Viscous Bidirectional Vortex," *Physics of Fluids*, Vol. 21, No. 10, October 2009, pp. 103603. doi:10.1063/1.3247186.
- [27] Shepherd, C. B. and Lapple, C. E., "Flow Pattern and Pressure Drop in Cyclone Dust Collectors," *Industrial & Engineering Chemistry*, Vol. 31, No. 8, August 1939, pp. 972–984. doi:10.1021/ie50356a012.
- [28] Shepherd, C. B. and Lapple, C. E., "Flow Pattern and Pressure Drop in Cyclone Dust Collectors Cyclone without Intel Vane," *Industrial & Engineering Chemistry*, Vol. 32, No. 9, September 1940, pp. 1246–1248. doi:10.1021/ie50369a042.
- [29] Alexander, R. M., "Fundamentals of Cyclone Design and Operation," Proceedings of the Australasian Institute of Mining and Metallurgy, No. 152–153, Australasian Institute of Mining and Metallurgy, 1949, pp. 203–228.
- [30] ter Linden, A. J., "Investigations into Cyclone Dust Collectors," *Proceedings of the Institution of Mechanical Engineers*, Vol. 160, No. 1, June 1949, pp. 233–251. doi:10.1243/pime_proc_1949_160_025_02.
- [31] Stairmand, C. J., "The Design and Performance of Cyclone Separators," *Transactions of the Institution of Chemical Engineers*, Vol. 29, 1951, pp. 356–383.
- [32] Prockat, F., Beitrag zur Kenntnis der Vorgange bei dertrockenen Aufbereitung und Abscheidung von Stauben, F. C. Glasser, Berlin, 1929.
- [33] Peterson, C. M. and Whitby, K. T., "Fractional Efficiency Characteristics of Unit Type Collectors," ASHRAE Journal, Vol. 7, No. 5, 1965, pp. 42–49.
- [34] Swift, P., "Dust Control in Industry 2," Steam Heat Engineering, Vol. 38, 1969, pp. 453–456.
- [35] Avant, R. V., Parnell, C. B., and Sorenson, J. W., "Analysis of Cyclone Separator Collection Performance for Grain Sorghum Dust," ASAE Winter Meeting, American Society of Agricultural and Biological Engineering St. Joseph, MI, ASAE Paper 76-3543, Chicago, IL, December 1976, p. 33.
- [36] Kelsall, D. F., "A Study of the Motion of Solid Particles in a Hydraulic Cyclone," *Transactions of the Institution of Chemical Engineers*, Vol. 30, April 1952, pp. 87–108.
- [37] Kelsall, D. F., "A Further Study of the Hydraulic Cyclone," *Chemical Engineering Science*, Vol. 2, No. 6, December 1953, pp. 254–272. doi:10.1016/0009-2509(53)80044-8.
- [38] Fontein, F. J. and Dijksman, C., Recent Developments in Mineral Dressing, Institution of Mining and Metallurgy, London, 1953.
- [39] Smith, J. L., "An Experimental Study of the Vortex in the Cyclone Separator," *Journal of Basic Engineering Transactions of the ASME*, Vol. 84, No. 4, December 1962, pp. 602–608. doi:10.1115/1.3658721.
- [40] Smith, J. L., "An Analysis of the Vortex Flow in the Cyclone Separator," *Journal of Basic Engineering Transactions of the ASME*, Vol. 84, No. 4, December 1962, pp. 609–616. doi:10.1115/1.3658722.

- [41] Leith, D. and Licht, W., "The Collection Efficiency of Cyclone Type Particle Collectors A New Approach," *AIChE Symposium Series*, Vol. 68, No. 126, 1972, pp. 196–206.
- [42] Leith, D. and Mehta, D., "Cyclone Performance and Design," *Atmospheric Environment* (1967), Vol. 7, No. 5, May 1973, pp. 527–549. doi:10.1016/0004-6981(73)90006-1.
- [43] Dabir, B. and Petty, C. A., "Measurements of Mean Velocity Profiles in a Hydrocyclone using Laser Doppler Anemometry," *Chemical Engineering Communications*, Vol. 48, No. 4-6, November 1986, pp. 377–388. doi:10.1080/00986448608910025.
- [44] Chu, L.-Y. and Chen, W.-M., "Research on the Motion of Solid Particles in a Hydrocyclone," Separation Science and Technology, Vol. 28, No. 10, July 1993, pp. 1875–1886. doi:10.1080/01496399308029247.
- [45] Hoekstra, A. J., Derksen, J. J., and van den Akker, H. E. A., "An Experimental and Numerical Study of Turbulent Swirling Flow in Gas Cyclones," *Chemical Engineering Science*, Vol. 54, No. 13-14, July 1999, pp. 2055–2065. doi:10.1016/s0009-2509(98)00373-x.
- [46] Derksen, J. J. and van den Akker, H. E. A., "Simulation of Vortex Core Precession in a Reverse-Flow Cyclone," AIChE Journal, Vol. 46, No. 7, July 2000, pp. 1317–1331. doi:10.1002/aic.690460706.
- [47] Derksen, J. J., "Separation Performance Predictions of a Stairmand High-Efficiency Cyclone," *AIChE Journal*, Vol. 49, No. 6, June 2003, pp. 1359–1371. doi:10.1002/aic.690490603.
- [48] Derksen, J. J., van den Akker, H. E. A., and Sundaresan, S., "Two-Way Coupled Large-Eddy Simulations of the Gas-Solid Flow in Cyclone Separators," *AIChE Journal*, Vol. 54, No. 4, April 2008, pp. 872–885. doi:10.1002/aic.11418.
- [49] Hu, L. Y., Zhou, L. X., Zhang, J., and Shi, M. X., "Studies on Strongly Swirling Flows in the Full Space of a Volute Cyclone Separator," *AIChE Journal*, Vol. 51, No. 3, March 2005, pp. 740–749. doi:10.1002/aic.10354.
- [50] Cortes, C. and Gil, A., "Modeling the Gas and Particle Flow Inside Cyclone Separators," *Progress in Energy and Combustion Science*, Vol. 33, No. 5, October 2007, pp. 409–452. doi:10.1016/j.pecs.2007.02.001.
- [51] Hussain, M., Mayur, K. M., Pradeep, D., Prithvi, B., and Srinivas, S., "Design and Analysis of Cyclone Separator," International Journal of Scientific and Engineering Research (IJSER), Vol. 11, No. 6, June 2020, pp. 207–212.
- [52] Zabala-Quintero, C., Ramirez-Pastran, J., and Torres, M. J., "Performance Characterization of a New Model for a Cyclone Separator of Particles Using Computational Fluid Dynamics," *Applied Sciences*, Vol. 11, No. 12, June 2021, pp. 5342. doi:10.3390/app11125342.
- [53] Sayed, M. A., Dehbi, A., Niceno, B., Mikityuk, K., and Krinner, M., "Flow Simulation of Gas Cyclone Separator at High Reynolds Number Using the Elliptic-Relaxation Hybrid LES/RANS (ER-HRL) Model," *Proceedings of the 6th World Congress on Momentum, Heat and Mass Transfer*, Avestia Publishing, June 2021. doi:10.11159/icmfht21.lx.110.
- [54] Fang, D., Majdalani, J., and Chiaverini, M. J., "Simulation of the Cold-Wall Swirl Driven Combustion Chamber," 39th AIAA/ASME/SAE/ASEE Joint Propulsion Conference and Exhibit, AIAA Paper 2003-5055, July 2003. doi:10.2514/6.2003-5055.
- [55] Murray, A. L., Gudgen, A. J., Chiaverini, M. J., Sauer, J. A., and Knuth, W. H., "Numerical Code Development for Simulating Gel Propellant Combustion Processes," *JANNAF*, May 2004.
- [56] Maicke, B. A. and Talamantes, G., "Numerical Investigation of Injection Variation in the Bidirectional Vortex," *AIAA Journal*, Vol. 55, No. 8, June 2017, pp. 2544–2554. doi:10.2514/1.j055807.
- [57] Talamantes, G. and Maicke, B. A., "Parametric Study of the Bidirectional Vortex through Outlet Variation," 53rd AIAA/SAE/ASEE Joint Propulsion Conference, AIAA Paper 2017-4753, July 2017. doi:10.2514/6.2017-4753.
- [58] ANSYS, "Fluent, Release 2020 R1, Version 18.1," 2020.
- [59] ANSYS Inc., Southpointe, 275 Technology Drive, Canonsburg, PA, ANSYS Fluent User's Guide, 15th ed., November 2013.
- [60] ANSYS, "ANSYS Fluent Mosaic Technology Automatically Combines Disparate Meshes with Polyhedral Elements for Fast Accurate Flow Resolution," White paper, Canonsburg, PA, November November 2018.
- [61] Sharma, G. and Majdalani, J., "Characterization of the Cyclonic Flowfield in a Swirl Driven Combustion Chamber," 53rd AIAA/SAE/ASEE Joint Propulsion Conference, AIAA Paper 2017-4667, July 2017. doi:10.2514/6.2017-4667.

- [62] Faler, J. H. and Leibovich, S., "Disrupted States of Vortex Flow and Vortex Breakdown," *Physics of Fluids*, Vol. 20, No. 9, 1977, pp. 1385–1400. doi:10.1063/1.862033.
- [63] Zhang, B., Guo, X., and Yang, Z., "Analysis on the Fluid Flow in Vortex Tube with Vortex Periodical Oscillation Characteristics," *International Journal of Heat and Mass Transfer*, Vol. 103, December 2016, pp. 1166–1175. doi:10.1016/j.ijheatmasstransfer.2016.08.063.
- [64] Wang, Y., Wang, X., and Yang, V., "Evolution and Transition Mechanisms of Internal Swirling Flows with Tangential Entry," *Physics of Fluids*, Vol. 30, No. 1, January 2018, pp. 013601. doi:10.1063/1.5001073.